January 2010

High-Speed Photoacoustic Microscopy In Vivo

Liang Song
Washington University in St. Louis

WASHINGTON UNIVERSITY

School of Engineering and Applied Science

Department of Biomedical Engineering

Dissertation Examination Committee:

Lihong Wang, Chair
Samuel Achilefu
Jeffrey Arbeit
Igor Efimov
Jean Schaffer
Younan Xia

HIGH-SPEED PHOTOACOUSTIC MICROSCOPY *IN VIVO*

by

Liang Song

A dissertation presented to the
Graduate School of Arts & Sciences
of Washington University in
partial fulfillment of the
requirements for the degree
Doctor of Philosophy

December 2010
Saint Louis, Missouri

Abstract

The overarching goal of this research is to develop a novel photoacoustic microscopy (PAM) technology capable of high-speed, high-resolution 3D imaging *in vivo*. PAM combines the advantages of optical absorption contrast and ultrasonic resolution for deep imaging beyond the quasi-ballistic regime. Its high sensitivity to optical absorption enables the imaging of important physiological parameters, such as hemoglobin concentration and oxygen saturation, which closely correlate with angiogenesis and hypermetabolism—two hallmarks of cancer.

To translate PAM to the clinic, both high imaging speed and high spatial resolution are desired. With high spatial resolution, PAM can detect small structural and functional changes early; whereas, high-speed image acquisition helps reduce motion artifacts, patient discomfort, cost, and potentially the risks associated with minimally invasive procedures such as endoscopy and intravascular imaging.

To achieve high imaging speed, we have constructed a PAM system using a linear ultrasound array and a kHz-repetition-rate tunable laser. The system has achieved a 249-Hz B-scan rate and a 0.5-Hz 3D imaging rate (over ~6 mm × 10 mm × 3 mm), over 200 times faster than existing mechanical scanning PAM using a single ultrasonic transducer. In addition, high-speed optical-resolution photoacoustic microscopy (**OR-PAM**) technology has been developed, in which the spatial resolution in one or two dimension(s) is defined by the diffraction-limited optical focus. Using section illumination, the elevational resolution of the system has been improved from ~300 μm to ~28 μm, resulting in a significant improvement in the 3D image quality. Furthermore, multiple optical foci with a microlens array have been used to provide finer than 10-μm lateral resolution—enabling the system to image capillary-level microvessels *in vivo*—while offering a speed potentially 20 times faster than previously existing single-focus OR-PAM. Finally, potential

biomedical applications of the developed technology have been demonstrated through *in vivo* imaging of murine sentinel lymph nodes, microcirculation dynamics, and human pulsatile dynamics. In the future, this high-speed PAM technology may be adapted for clinical imaging of diabetes-induced vascular complications or tumor angiogenesis, or miniaturized for gastrointestinal or intravascular applications.

Acknowledgement

I am deeply indebted to Professor Lihong Wang, my mentor, for his guidance, help, support, and encouragement. Being a great scientist himself, he has taught me not only the knowledge and technical skills for rigorous academic research, but also an analytical and always positive approach to tackling challenging problems.

I sincerely thank all my committee members, Professors Samuel Achilefu, Jeffrey Arbeit, Igor Efimov, Jean Schaffer, and Younan Xia, for taking their invaluable time to advise and guide my research. I am grateful to Professor K. Kirk Shung and his group at the University of Southern California for providing us the high-frequency ultrasound array.

I would like to thank my Optical Imaging Lab colleagues and friends, Changhui Li, Manojit Pramanik, Chulhong Kim, Song Hu, Junjie Yao, Christopher Favazza, Joon-Mo Yang, Hui Fang, Xinmai Yang, Lidai Wang, Zijian Guo, and Bin Rao for stimulating and beneficial discussions. I am particularly grateful to Dr. Roger Zemp for helping me get started on my research project, and Dr. Konstantin Maslov for his constant advice, critiques, and help on the design and implementation of my systems. I am also grateful to Professor James Ballard for his constant help with manuscript writing. I thank all other Optical Imaging Lab members for their assistance and friendship.

This work was sponsored in part by National Institutes of Health grants (principal investigator: Lihong Wang) R01 EB000712, R01 EB008085, R01 CA134539, U54 CA136398, and R01 EB010049.

I would like to dedicate this dissertation to my parents, for their unconditional love, support, and encouragement all the time.

Table of Contents

Chapter 1 Introduction

This project aims to develop a novel photoacoustic microscopy (**PAM**) technology capable of high-speed, high-resolution 3D imaging *in vivo*. PAM is extremely sensitive to optical absorption contrast, which correlates with important physiological parameters such as the concentration and oxygen saturation of hemoglobin [1]. Such parameters are closely related to angiogenesis and hypermetabolism, two hallmarks of cancer [2]. As a result, PAM has broad potential applications in biomedicine, including the early diagnosis of cancer.

In PAM, both imaging speed and spatial resolution are important. A high spatial resolution (<100 μm) enables PAM to resolve fine structural and functional changes (e.g., microcirculation dynamics), and thus to detect diseases early. A high imaging speed enables PAM to (1) reduce motion artifacts that are due to, for example, breathing of the subjects, (2) reduce cost and patient discomfort, (3) image and study physiological dynamics, (4) perform high-throughput preclinical imaging (critical in drug development), and (5) potentially reduce risks associated with minimally invasive procedures (e.g., endoscopy) in clinical practice. Consequently, this research will open up many new possibilities for PAM. In the future, this high-speed, high-resolution PAM technology may be applied to study tumor angiogenesis and diabetes-induced vascular complications; it may also be miniaturized for intracoronary imaging of vulnerable plaques and early diagnosis of gastrointestinal cancer.

1.1 Need for new imaging technologies

Traditional diagnostic imaging technologies—including ultrasound, X-ray computed tomography (CT), and magnetic resonance imaging (MRI)—have dramatically improved patient care in the

clinic. Recently, they have also been scaled down to allow high-resolution imaging of small animals *in vivo*, which is important to both gaining a better understanding of diseases and developing effective therapeutics [3-6]. However, they have either limited sensitivity or spatial resolution (or both) in detecting small lesions and early physiological changes induced by cancer and many other diseases.

Optical imaging has recently emerged as both a vital preclinical research tool (e.g., two-photon microscopy of *in vivo* brain functions [7]) and an effective clinical diagnostic technique (e.g., optical coherence tomography for the diagnosis of eye diseases [8, 9] and coronary heart disease [10-12]). In general, optical imaging technologies complement the traditional imaging modalities with several unique and attractive features:

1. Optical imaging with visible and near infrared (NIR) light is non-ionizing, and thus safer than imaging modalities using X-rays—which have photon energies of thousands of eV and may cause carcinogenesis;
2. Optical absorption is related to various intrinsic contrast origins, such as oxy- and deoxy-hemoglobin, melanin, lipids, and even water, which enables optical imaging to map physiological parameters with high sensitivity;
3. Multi-wavelength measurements allow simultaneous quantification of both the concentration and oxygen saturation of hemoglobin, offering functional imaging of angiogenesis and hypermetabolism;
4. A wide range of exogenous optical absorption contrast agents is available for optical molecular imaging.

However, a fundamental challenge in optical imaging has been achieving high spatial resolution with deep penetration. Because of the strong optical scattering in biological tissue,

existing high-resolution optical imaging technologies relying on the detection of ballistic photons cannot penetrate beyond the optical transport mean free path. For example, confocal microscopy can achieve ~1-μm resolution but can penetrate only 0.5 mm into scattering biological tissue [13], whereas OCT can achieve ~10-μm resolution but can penetrate only ~1 mm [14]. In addition, as none of them sense optical absorption directly, exogenous contrast agents—which might be toxic—are usually needed for functional imaging. While diffuse optical imaging can penetrate a few centimeters and provide functional information such as oxygen saturation of hemoglobin, its spatial resolution is rather poor (~a few millimeters) [15]. Therefore, new technologies are urgently needed to meet this challenge. Among emerging novel technologies, photoacoustic microscopy is a strong candidate, due to its capability to image optical absorption contrast with high spatial resolution at depths beyond the optical transport mean free path.

1.2 Fundamentals of photoacoustic imaging

The photoacoustic effect describes the generation of acoustic waves upon absorption of photons. Though Alexander Graham Bell discovered this effect as far back as 1880 [16], it was not until the early 1990s—after the technological advances of lasers, computers, and computed tomography—that its medical applications started to become apparent [17, 18]. When a short laser pulse is absorbed by structures (such as microvessels) in biological tissue, wideband ultrasonic (photoacoustic) waves are produced from a thermal- and stress-confined thermoelastic expansion [19]. Photoacoustic signals are then detected and reconstructed to form an image. The image signal amplitude is related to the optical absorption and the Grueneisen parameter. In photoacoustic imaging, both ballistic and diffuse photons are utilized to generate photoacoustic signals, and the spatial resolution is determined primarily by ultrasonic rather than optical parameters. Since ultrasonic scattering in biological tissue is two to three orders of magnitude

weaker than optical scattering, high spatial resolution can be achieved at depths beyond the optical transport mean free path.

In general, if the laser excitation is in both thermal and stress confinements, the initial local photoacoustic pressure rise p_0 can be described by [20]:

$$p_0 = \Gamma \eta_{th} A = \Gamma \eta_{th} \mu_a F, \qquad (1.1)$$

where Γ denotes the dimensionless Grueneisen parameter, *A* the specific optical energy deposition (J/cm^3), η_{th} the percentage of *A* converted into heat, μ_a the optical absorption coefficient (cm^{-1}), and *F* the optical fluence (J/cm^2). It can be seen that p_0 depends on the optical energy deposition as well as the thermal and mechanical properties of the tissue. In soft tissue imaging, Γ and η_{th} are usually treated as constants, and thus the initial pressure rise reflects essentially the optical energy deposition ($\mu_a \times F$).

In biological tissue, the primary endogenous chromophores are oxy- and deoxy-hemoglobin (**HbO_2** and **HbR**) and melanin. The strong intrinsic absorption of HbO_2 and HbR in the visible spectrum enables blood vessels to be readily photoacoustically imaged noninvasively with high contrast and without using ionizing radiation. Using multi-wavelength measurements, changes in both the concentration and oxygen saturation of hemoglobin can be quantified. Hence, photoacoustic functional imaging of endogenous hemoglobin contrast is available with both high sensitivity and high spatial resolution at large depths.

1.3 Photoacoustic microscopy using an ultrasound array

Existing high-resolution purely optical imaging technologies—including confocal microscopy [13], two-photon microscopy [21], and optical coherence tomography (**OCT**) [14]—have had a profound impact on biomedicine. However, since none of them sense optical absorption directly, label-

free functional imaging is not easily available with these modalities. Furthermore, they rely on the detection of ballistic photons, and thus cannot image beyond the optical transport mean free path (~1 mm in human skin) [20].

Photoacoustic microscopy overcomes the limitations of existing high-resolution optical imaging technologies and combines excellent optical contrast with high ultrasonic resolution at depths beyond the quasi-ballistic regime. In addition, the maximum imaging depth and the spatial resolution of PAM can be scaled with its ultrasonic parameters [22]. PAM is emerging as a viable technology for both clinical and preclinical imaging and has demonstrated potential for many biomedical applications, including the imaging of single vessel oxygenation [23], quantification of tumor hypoxia [24], and detection of amyloid plaques [25].

The development of PAM using a high-frequency ultrasound array may lead to important advances [26], including:

1. The potential for high-speed and even real-time imaging, which is valuable to both clinical practice and preclinical research. In the clinic, time is critical, and in order to make decisions promptly, there is an increasing demand for real-time imaging. In preclinical research, such as small animal imaging for drug development, high-throughput is a major goal, and thus high-speed imaging is very much desired. In addition, high-speed imaging is important for studying various physiological dynamics.
2. The potential for high spatial resolution, which is crucial to image the microvessels (usually <100 μm in diameter) in microcirculation. Since the spatial resolution in PAM is primarily determined by the ultrasonic frequency bandwidth, high-frequency ultrasound is required for high-resolution imaging.

3. The potential for large depth of field. While single-element PAM has a relatively small predefined depth of field with high resolution, ultrasound array PAM with dynamic focusing will enable a large depth of field for high-resolution imaging.
4. The potential to build a handheld imaging device. A PAM system based on an ultrasound array has a relatively small physical footprint, and can potentially be built into a handheld imaging device.
5. The potential to leverage commercial diagnostic ultrasound instruments. Most modern diagnostic ultrasound instruments are based on array technologies. Therefore, for clinical use, it will be valuable if we can leverage existing commercial ultrasound platforms to develop novel PAM technology, which could be more easily accepted by physicians.

1.4 Summary

This dissertation focuses on the development of novel PAM technologies using a high-frequency ultrasound array for high-speed, high-resolution 3D imaging *in vivo*.

Chapter 2 presents our development of a real-time PAM system.

Chapter 3 demonstrates the use of the real-time PAM system to image murine cardiovascular dynamics *in vivo*.

Chapter 4 presents our development of a fast 3D dark-field reflection-mode PAM system.

Chapter 5 demonstrates the use of the fast 3D PAM system to noninvasively identify and image the dynamics of sentinel lymph nodes *in vivo* in a murine model.

Chapter 6 demonstrates the use of an improved 3D PAM system to image human pulsatile dynamics *in vivo*.

Chapter 7 presents our development of a section-illumination PAM system capable of imaging the microcirculation dynamics *in vivo*.

Chapter 8 presents our development of a multi-focal optical-resolution PAM system capable of imaging hemoglobin concentration and oxygenation in capillary-level microvessels *in vivo* at high speed.

Chapter 9 summarizes this dissertation.

Chapter 2 Real-time Photoacoustic Microscopy *In vivo*[†]

2.1 Introduction

Modern diagnostic imaging methods offer clinicians the ability to non-invasively visualize anatomy and judge pathology based on tissue morphology. While anatomical visualization has served the biomedical community well, there has been much recent progress in imaging methods providing molecular and functional information [27]. The surge of biomedical research spawned by the completion of the human genome project is opening new windows of opportunity for bio-imaging in medicine to elucidate genotype-phenotype relationships. Since mice possess surprising genetic homology with humans, they have emerged as an important means of studying disease, and many imaging techniques have evolved specifically for imaging small animals. Such small animal imaging modalities are accelerating biomedical research and enabling longitudinal studies in the same animal over time, rather than necessitating a population of animals sacrificed at various time points, thus avoiding the statistical plague of inter-subject variability [28].

In the clinic, time is critical and there is an increasing demand for real-time imaging techniques for immediate operator-feedback. Because modern ultrasound systems offer real-time imaging capabilities, ultrasound is one of the most widely used clinical imaging modalities.

A major goal in small animal imaging is high throughput. The recent emergence of a small-animal high-frequency ultrasound imaging system has seen significant attention and been used by researchers in various fields, and has generated a large number of studies. While primarily providing real-time anatomical imaging capabilities, color Doppler mode also enables functional

[†] Reused with permission from R. J. Zemp, L. Song, R. Bitton, K. K. Shung, and L. V. Wang, "Realtime photoacoustic microscopy *in vivo* with a 30-MHz ultrasound array transducer," *Optics Express* **16**, 7915 (2008).

visualization of blood flow, and increasingly quantitative estimates of blood velocities. Microbubbles [29] and perfluorocarbon nanodroplets [30] are being pursued as molecular imaging ultrasound contrast agents, offering potentially very high sensitivity.

Recently, high-frequency ultrasound has seen a successful union with optical imaging techniques in the form of photoacoustic imaging [19]. In photoacoustic imaging, nanosecond laser pulses incident on tissue generate acoustic signals due to thermal- and stress-confined thermoelastic expansion in subcutaneous absorbing structures such as microvessels. Photoacoustic signals are detected and reconstructed to form images of optical absorption. Since whole blood is over two orders of magnitude more absorbing than surrounding tissue for much of the visible spectrum, very high image contrast is attained. Because spatial resolution in photoacoustic imaging is determined primarily by ultrasonic rather than optical parameters, multiply scattered light is tolerated. This is noteworthy since imaging depth beyond a transport mean free path is possible, unlike approaches relying on minimally scattered photons, such as traditional optical microscopy methods and optical coherence tomography.

While diffuse-optical tomographic methods permit and rely on multiply-scattered light, their reconstruction methods are ill-posed, transport-regime reconstruction is challenging [31, 32], and fine spatial resolution is practically difficult to obtain due to factors such as regularization. Analogous to computed tomography, circular-scanning photoacoustic tomography (PAT) has been used for non-invasively visualizing small animal brains [33], including application to functional brain imaging [34]. More recently, Maslov et al [35] and Zhang et al [1] have demonstrated exquisite images of subcutaneous microvasculature using dark-field confocal photoacoustic microscopy (PAM), a raster-scanning-based reflection geometry imaging system. Unique to photoacoustic methods is the ability to image blood oxygen saturation as well as concentration

of total hemoglobin [1, 36, 37]. Emerging photoacoustic methods are enabling molecular imaging in small animals, including imaging of gene expression [38] and cell receptors [24]. Unfortunately, long scan times are presently required in both scanning PAT and PAM.

Our goal was to construct a real-time high-frequency photoacoustic imaging system. In principle, using an ultrasound array transducer, a photoacoustic image can be formed from each laser shot by reconstructing photoacoustic signals received in parallel through array elements. The system described in this article approaches this goal but rather uses a small number of laser shots at a high-repetition rate to acquire signals in multiplexed mode. Even with the present multiplexing scheme, our system offers real-time performance.

While Niederhauser et al [39] used an array system to demonstrate photoacoustic imaging, their system lacked real-time imaging capabilities, primarily due to the 10-Hz repetition rate of their laser system. Moreover, they used only 16 receive elements to form an image using a diagnostic frequency ultrasound array. Others [40-43] have also demonstrated the use of arrays for photoacoustic imaging, however for low diagnostic frequencies. Optical detection of ultrasound using Fabry-Perot etalons has led to emerging 2D arrays, recently producing 3D microvascular images in animals and human subjects [44]. While this technique offers considerable promise, the signal-to-noise ratio strongly depends on the laser power of a laser probe beam, and presently this often means the necessity of scanning the probe beam, necessitating many pulsed laser excitations, and sacrificing real-time performance. A high-frequency array system for photoacoustic microscopy was previously reported by our group [45], but real-time acquisition and display was lacking. To our knowledge, this is the first published report of a real-time high-frequency photoacoustic imaging system. We will demonstrate the real-time imaging capabilities of our system, quantify its performance, and present *in vivo* data.

2.2 Methods

Our system consists of a laser diode-stack pumped Nd:YLF Q-switched laser, a tunable dye laser, a high-frequency ultrasound array transducer, custom receive and control electronics, an 8-channel PCI digitizer, a multi-core PC, and an LCD monitor for real-time display. A diagram of the main components of the system is shown in Figure 2.1. We will describe each main component below.

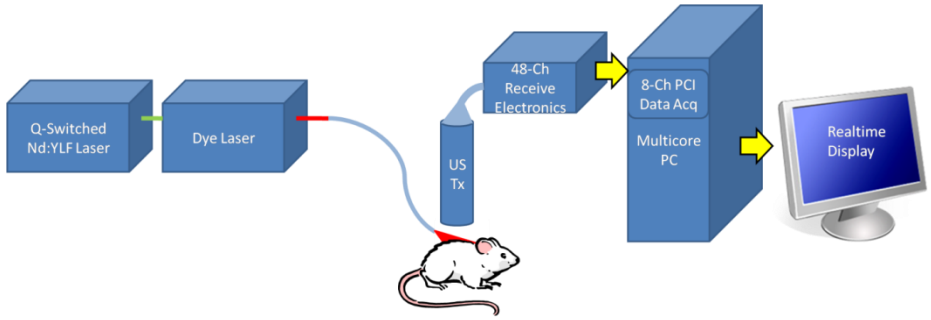

Figure 2.1. Diagram of the key components of our real-time photoacoustic imaging system, including a KHz-repetition rate Q-switched pump laser, a dye laser, a fiber optic cable, an ultrasound transducer (US TX), receive electronics, a dual-socket quad-core CPU personal computer (PC) with an 8-Ch 125 MS/s data acquisition card, and a monitor for real-time display.

2.2.1 Optics

A Nd:YLF diode-pumped Q-switched laser (INNOSLAB, Edgewave GmbH, Germany) was used to produce 7-ns optical pulses of ~12 mJ at a wavelength of 523 nm. Optical pumping by continuous-wave laser diode stacks in our Nd:YLF laser provides the flexibility of external triggering on demand at rates up to 1 KHz, without pulse energy loss. For our imaging system, this feature is a significant advantage over flashlamp-pumped Q-switched lasers that typically must be maintained at a fixed pulse repetition rate, and typically support much lower pulse rates. This laser was used to pump a dye laser (Cobra, Sirah Laser –und Plasmatechnik GmbH,

Germany) outfitted with a high flow-rate dye circulator to minimize photo-depletion of the dye at high-repetition rates. The tunable output of the dye laser (with Pyrromethene 597 laser dye) enabled peak output power at 578 nm with a roughly 30-nm tuning range. At the isosbestic 570-nm wavelength (where oxy- and deoxy-hemoglobin have equal molar extinction coefficients), the 1/e attenuation length of light in whole blood is roughly 40 μm, hence a photoacoustic signal from a blood vessel should possess a bandwidth of roughly 37 MHz, which closely matches our 30-MHz ultrasound transducer's center frequency. The 2-3 mJ of dye laser output were coupled into a 600-μm optical fiber and light from the other end of the fiber was delivered obliquely past the ultrasound transducer array forming an oblong pattern on the skin along the array axis. The estimated fluence was 5 – 10 mJ/cm^2 per pulse, below the ANSI recommended Maximum Permissible Exposure of 20 mJ/cm^2. For our imaging experiments we used 578-nm and 570-nm wavelengths corresponding to the peak dye laser power and an isosbestic point, respectively.

2.2.2 High-frequency ultrasound array transducer

While diagnostic medical ultrasound systems typically operate in the 1–15 MHz range, the development of array systems with higher operating frequencies is more challenging and still in the research phase. Difficulties include fabricating arrays with small kerfs, interconnect issues, weak capacitive impedance of small elements, crosstalk, noise, and lack of adequate receive electronics. While higher frequencies promise finer imaging resolution, attenuation limits penetration.

To receive photoacoustic signals, we used a unique 30-MHz linear array transducer fabricated from a 2-2-piezo-composite by the NIH Transducer Resource Center at the University of Southern California [46]. The advantage of the piezocomposite material used in our application

is that it offers high piezo-electric properties (important for transducing weak photoacoustic signals) while the acoustic impedance of the material is greatly improved compared to pure piezoceramics [46].

Our array possessed 48 elements with 100-μm pitch, 19.1 dB compensated pulse-echo insertion loss, and element cross-talk less than -25 dB. A fixed 8.2-mm elevation focus was provided, with elements possessing 2-mm height. While the mean pulse-echo fractional bandwidth was 50%, this figure was improved to ~70% for receive only, used for our present photoacoustic imaging system.

2.2.3 Data acquisition and control electronics

Photoacoustic signals converted to voltage signals by the ultrasound array were amplified and conditioned prior to digitization. The 48 receive channels of the system were each amplified by pre-amplifiers (MAX4107, Maxim/Dallas Semiconductor), down-multiplexed 3:1 using RF multiplexer ICs (AD8184, Analog Devices), bandpass filtered with a 4^{th}-order Butterworth filter, then amplified using a 40-dB variable gain amplifier (AD8332, Analog Devices). RF transformers (T1 6T, Minicircuits) are used to convert the differential output of the variable gain amplifiers to a single line and a final 23-dB fixed gain stage offers a total variable gain between 33 and 73 dB. All these steps were implemented on an RF printed circuit board having 48 SMA inputs and 16 SMA outputs, described by Bitton et al [47]. The remaining 16 channels were down-multiplexed to 8 channels using modified MAX4141 multiplexer evaluation boards (Maxim, Inc). The final 8 lines were digitized at 125 Mega-sample-per-second using a 14-bit 8-channel PCI data acquisition card (Octopus CompuScope 8389, GaGe Applied Systems, USA). SMA-terminated RG-174 coaxial cables connected the array to the RF receiver board, the receiver board to the additional multiplexers, and the multiplexers to the data acquisition card. The PCI digitizer

board was controlled using custom software written in C and C#, modified from the manufacturer's software development kits. The card had 128-MB on-board memory, and the PCI bus offered 32-bit transfers at 66-MHz clock rates, providing data transfer to the PC RAM at better than 200 MBPS. Benchmark software written in C showed the system capable of sustained data acquisition and transfer to PC RAM for 1 KS records at roughly 1 KHz. The card was used as the master clock for our entire system, and was programmed to send out trigger signals to the multiplexer control and laser. In this way each laser trigger was guaranteed to be synchronized with the data acquisition clock, avoiding pulse-to-pulse jitter detrimental to multiplexed beamforming. For each B-frame to be acquired, the Gage card was programmed to record a sequence of 6 acquisitions, enabling multiplexed access to 48 array elements with 8 receive channels. Each acquisition was preceded by a trigger out signal with a specified delay time before recording. The repetition rate of the 6 acquisitions per B-frame, and accompanying trigger signals was set at 1-KHz, determined by the Gage card hardware, with the precision of the onboard 125 MS/s clock. The inter-frame delay, however, was software controlled, and hence variable due to lack of interrupt control in the Windows operating system. Our hypothesis was that since a B-frame was acquired in only 6 ms, beamforming degradation due to motion over multiplexed data acquisition should be minimal. This hypothesis is addressed in the Results section.

The multiplexer control circuit consisted of a simple 4-bit counter, counting from binary 0 to 5. The counter was implemented using CMOS pre-settable counter integrated circuits (CD74HCT163E, Texas Instruments). At the beginning of the data acquisition cycle, parallel-port signals were used to toggle counter resets and count enables. Two bits of the counter output were used to control the 3 multiplexed states of the RF board, and a third bit was used to

control the 2:1 MUX boards, as illustrated in Figure 2.2. Trigger signals from the Gage card acted as the clock-input to the counter circuit, advancing the count, and changing the multiplexer state. A bit from the parallel-port was used to enable this trigger signal to pass to the laser via a D-latch. Since the Gage card's trigger out duration was too brief to reliably trigger the laser, a pulse-delay generator (DG535, Stanford Research Systems) was used to forward the trigger to the counter circuit with an expanded pulse width.

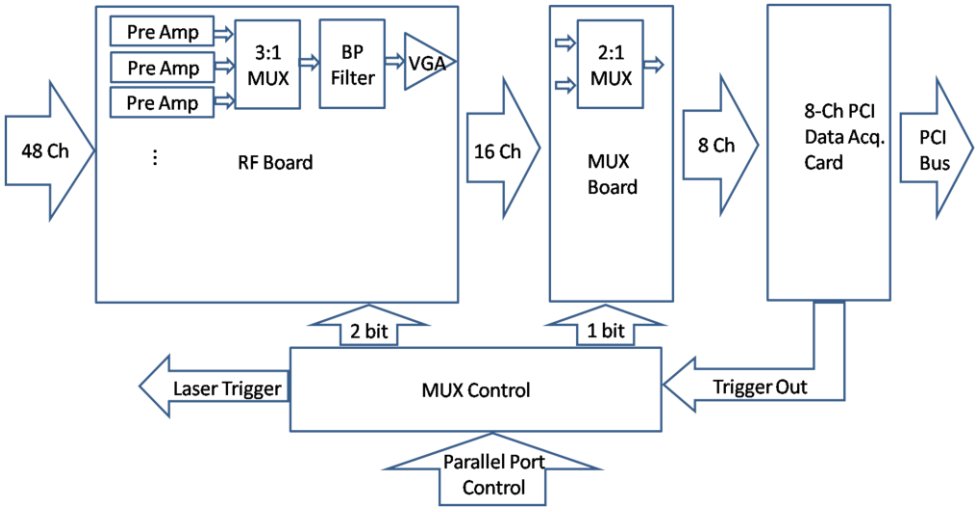

Figure 2.2. Architecture of the receive and control electronics of our real-time photoacoustic imaging system. The 48 receive channels are boosted by pre-amplifiers, down-multiplexed (MUX), bandpass (BP) filtered, and amplified with a variable gain amplifier (VGA) stage. The resulting 16 channels are down-multiplexed to 8 channels for digitization. Control electronics toggle through multiplexer states, and pass trigger signals to the laser.

2.2.4 Multi-threaded multi-core processor approach to parallel beamforming

While ultrasound beamforming traditionally uses hardware such as application-specific integrated circuits (ASICs), or programmable hardware such as field programmable gate arrays (FPGAs) [48, 49], we instead explore multi-core processors for this task. This approach will allow off-

the-shelf PCs to perform tasks that previously required dedicated hardware. Following Moore's 1965 projection that transistor densities will double every 18 – 24 months [50], and noting the recent trend in multi-core processors, we project that the software approach to beamforming may prove fruitful. Advantages include short high-level software development time, great flexibility for channel-domain processing, and post-beamforming signal and image processing, and ease of upgrading to new processor powers.

Dynamic receive beamforming was implemented in C++ and compiled to a Dynamic Link Library in Visual Studio 2005 Professional Edition (Microsoft Corp.). Multi-threaded parallel programming was accomplished by using OpenMP programs before 'for' loops for each A-scan reconstruction, along with the appropriate variable scope declarations. OpenMP is a collection of instructions simplifying the shared-memory multi-threading and parallel programming process. Our beamforming algorithm leverages the computing power of our multi-core processors by parallel computation of A-scans of different scan angles. Delay values for the dynamic receive beamforming algorithm were computed once prior to all beamforming computations, and stored in memory similar as an effective look-up table. Since our sampling rate is close to the Nyquist limit which is sparse for delay and sum beamforming operations, channel data was up-sampled 5 times using simple linear interpolation prior to beamforming. During beamforming, channel-data was delayed by pre-computed values, using nearest neighbor interpolation. Delays were computed as

$$\tau_n(R,t) = \frac{x_n \sin\theta}{c} + \frac{x_n^2 \cos^2\theta}{2Rc}, \qquad (2.1)$$

where x_n is the distance to the array element from the center of the array, c is the speed of sound, and θ is the desired steering angle. All 48 receive channels were used for each A-line in the beamformed image.

All operations were performed with pointers, abating the need for duplicate copies of data in the memory, and accelerating performance. Built-in compiler options were selected to optimize for speed. Benchmark tests beamforming 48 channels of 500 samples per channel into an image with 128 scan lines 500 samples deep were clocked at better than 83 frames per second on a fast PC (Dell Precision 490) with two 2.66 GHz Quad-core Xeon processors (with 8 MB of L2 cache and 1333 MHz front-side bus). The system possessed 4 GB of DDR2 SDRAM with a 667 MHz bus clock. This shared memory 8-core processor system represented one of the market's highest computing-power desktop PCs available at the time of this work (spring 2007). While the Xeon processors support 64-bit operations, the Gage card drivers were only available for 32-bit Windows and thus the available addressable RAM was limited to ~3 GB rather than the available 4 GB. It may be possible to significantly improve the 83 fps benchmark speed by further optimizing the beamforming algorithms using processor-specific assembly-language.

2.2.5 GPU-based scan conversion and display

Scan conversion refers to the process of mapping a matrix of beamformed data onto an appropriate curvilinear geometry. Scan conversion is often done with dedicated hardware, but may also be done with software. Since we wanted to reserve computing power for beamforming throughput, similar to [48], we decided to implement scan conversion and display using the Graphical Processing Unit (GPU) of the graphics card (128 MB PCIe x16 nVidia Quadro NVS 285) rather than the multi-core Central Processing Unit (CPU). Besides offloading computational burden from the CPU, GPU-based scan conversion allowed us to take advantage of a wide range of software tools for rendering graphics.

We used a novel approach to our scan conversion algorithm. Instead of computing each pixel of the curvilinear image by interpolation via a point-by-point coordinate transformation as

is typically done, we rather instructed the graphics card to warp our pre-scan-converted image matrix onto a 32×32 or 64×64 mesh of triangles defining the curvilinear coordinates, shown in Figure 2.3. This mesh was generated and stored in the graphics card memory prior to data streaming. The B-scan-images following beamformation were then written to the GPU in RGB-format and were then stretched onto the triangle mesh and displayed in the correct curvilinear format upon rendering. A new texture (pre-scan-converted B-mode image) was written to the GPU for each new frame. Zoom and pan capabilities were simply accomplished by keyboard-control of a virtual camera position above the scan-conversion mesh. Additionally, this approach provided vector-based rather than pixel-based rendering, offering smoothed rather than pixilated-looking images.

To implement these procedures, we used Microsoft XNA Game Studio in the Visual Studio C# Express Edition (Microsoft Corp.) environment. XNA is a new wrapper around the native Managed DirectX. Due to a well developed library, and graphic card-independent programming capabilities, this environment allowed rapid development of the rendering methods needed for real-time display. There are also some disadvantages. The use of pointers in C# is allowed but un-natural due to C#'s managed dynamic memory allocation and 'garbage' collector. Thus all CPU operations requiring speed were developed using C/C++ and these functions were compiled to Dynamic Link Libraries (DLLs), which were then called in the C# environment in the context of a so-called 'unsafe' scope.

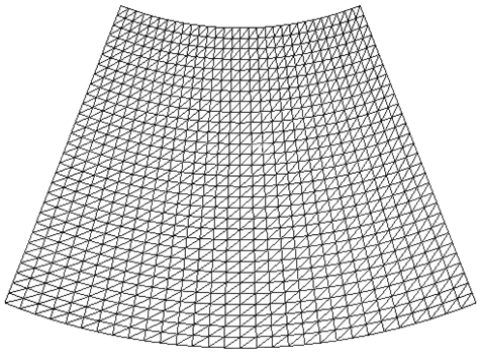

Figure 2.3. To offload computational burden from the CPUs to the GPU, we implemented a 32x32 scan-conversion mesh over which the pre-scan converted beamformed image was warped using graphic-card rendering methods primarily developed for the video game industry.

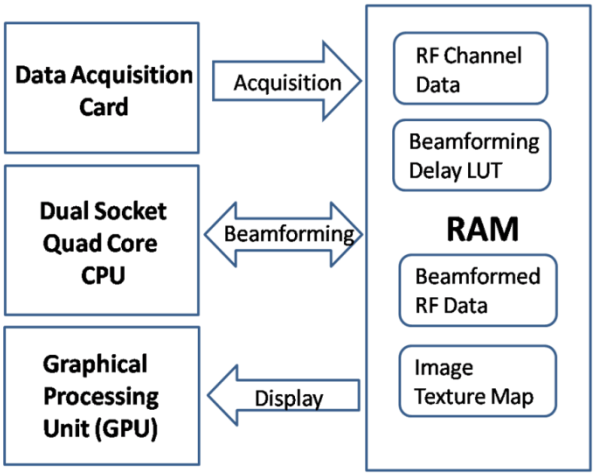

Figure 2.4. Schematic of software communication between the data acquisition card, CPUs, GPU, and system RAM. Note that the acquisition, beamforming, and display operations were implemented on parallel threads. Since these operations read and write common resources, signaling flags were used to avoid access conflicts.

2.2.6 Parallel threading issues

Multiple parallel threads are instantiated in our software: one for data acquisition and transfer, another for beamforming, another for scan conversion and display, and another for a graphical user interface enabling data logging and display options. Daughter threads are also spawned

from the beamforming thread via OpenMP to enable parallel reconstruction of A-scan lines as described above. If one process encounters an execution bottleneck, the other threads will continue to operate using the data available in the current state. Figure 2.4 shows how our software is organized to communicate between the PCI card, the CPUs, the GPU and the RAM. Note that some processes spawned on parallel threads require access to common data. Access to thread-sensitive resources is mediated by event-handling flags which are set and reset after each process completes its intended job. In this way potential conflicts between multiple threads are avoided.

2.2.7 Data archival and post-processing

Pre-beamformed channel data was archived to hard-disk for offline processing. A library of utility programs written in C++ and C# were used to perform rapid beamforming on archived data, and the post-beamformed RF data was written to file for envelope detection, scan conversion, and post-processing in MATLAB (Mathworks Inc). Post-processing operations included intensity transformations such as contrast stretching, and median filtering for edge-preserving noise reduction.

2.2 Results

2.2.1 Resolution study

To evaluate the system resolution, we constructed a phantom consisting of two crossed 6-μm-diameter carbon fibers suspended in water. Using a translation stage to move the probe relative to the phantom, we acquired images at progressive scan positions along the array's elevation direction. The maximum intensity C-scan projection image of the phantom is shown in Figure 2.5(a). A representative B-scan near the dashed line location is shown in Figure 2.5(b), and the

maximum cross-range photoacoustic amplitude of this B-scan is shown in Figure 2.5(c). These images demonstrate clearly distinguishable points separated at only ~80 μm (40 μm lateral separation and 70 μm vertical separation). At 6.9 mm imaging depth (normal depth from the transducer surface), the lateral resolution should be the product of the *f*# (6.9 mm / 4.8 mm = 1.44) times the center wavelength (50 μm), equal to 72 μm. The axial resolution, as measured in [45], was ~25-30 μm. Thus the clear 80 μm separation of carbon fibers is reasonable.

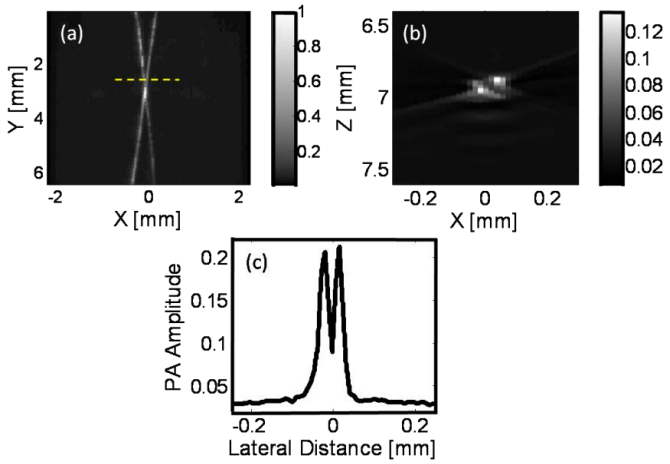

Figure 2.5. (a) C-scan maximum amplitude projection image of crossed 6-μm carbon fibers, constructed from 50 parallel B-scans. (b) Sample B-scan at the dotted-line position in (a). The carbon fibers are separated here by only ~80 μm, yet are clearly distinguishable. (c) Cross-range maximum amplitude projection of (b) onto the x-axis.

2.2.2 Frame rate

Our software enabled the following three modes of operation: (1) high-speed acquisition but with no real-time display (2) real-time acquisition and display, and (3) real-time acquisition and display with continuous hard-disk data logging. In high-speed acquisition mode (1), the frame rate could be as high as 167 frames per second (1000 Hz divided by 6 laser shots per image). In this mode, the number of frames that could be acquired was limited by the memory depth of

the data acquisition card. This mode may be valuable for studying small animals or embryos with very high heart rates. At 1000-Hz sustained repetition rate laser safety may be a concern as will be discussed. In mode (2), real-time acquisition and display, average frame rate was ~50 frames per second (fps). In mode (3) with continuous hard-disk data logging, frame-rate reduced to ~21 fps for ASCII file archival, but remained ~50 fps for binary formats. These results were obtained using an 80 GB SATA hard drive with an 8 MB cache and up to 3 GB/s transfer speed at 7200 rotations per minute. To verify the frame rate and to assess the inter-frame delays, an image frame trigger was recorded on an external oscilloscope (TDS5034, Tektronix). The frame trigger was obtained by taking the laser trigger signal and using a pulse-delay generator (DG535, Stanford Research Systems, Sunnyvale, CA) to produce a 7-ms-duration TTL pulse. Since each frame acquisition required a burst of 6 TTL laser triggers at 1-kHz repetition rate, with 7-ms hold-off time, the pulse-delay generator produced one image trigger per laser-trigger burst.

2.2.3 Evaluation of handheld performance

Because our data acquisition is multiplexed, we must realize that motion may not be tolerated if it is very fast. In particular, if we want the delay-and-sum beamforming computations to maintain coherence, inter-acquisition motion should be minimal, otherwise artifacts may be produced. By requiring that motion over our 6-ms acquisition time is less than ~$\lambda/4$, we restrict ourselves to motions with velocities of less than ~2 mm/s. While this velocity is small, we can also realize that our field of view with appreciable signal-to-noise is only ~4 mm by 4 mm. Hence this velocity represents translation across half the field of view in 1 second.

To test the performance of the system against motion for handheld operation, we imaged a 100-μm human hair while translating the array. We performed this translation using hand motion but restricting motion to vertical and horizontal translations by means of an optical post-

based translation guide. Movies of acquired photoacoustic images of the hair phantom demonstrating ~3 mm/s horizontal and vertical motions are shown in Figure 2.6 and Figure 2.7, respectively. No apparent distortion of the hair point-spread function was apparent. Note that images of the hairs appear to have a top and bottom lobe. This can be explained by noting that the top and bottom of the hair can be resolved with this system since the axial spatial resolution is ~25 μm.

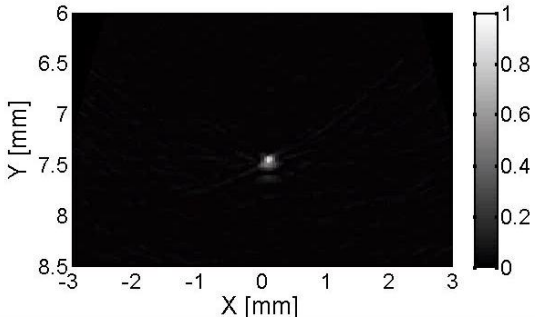

Figure 2.6. Movie (2.5 MB) of photoacoustic B-scans of a human hair in water. The probe was moved up and down in an oscillating fashion using manual adjustment of a micrometer on a translation stage. This video sequence demonstrates the real-time capability of the system, specifically it's robustness to vertical motions.

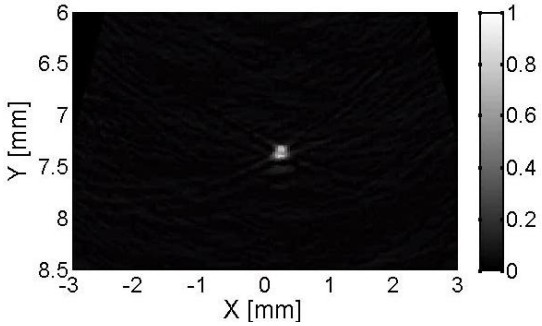

Figure 2.7. Movie (3 MB) of photoacoustic B-scans of a human hair in water. The probe was moved laterally by hand along a guide rail. This video sequence demonstrates the robustness of the multiplexed acquisition scheme against horizontal motions.

2.2.4 *In vivo* depth performance

To test *in vivo* performance, we imaged the upper thoracic region of young athymic nude mice (~10 g, Charles River). In doing so we fixed the transducer using a custom holder, and placed it in a de-ionized water bath, beneath which we placed a nude mouse. Consumer-grade plastic wrap coated the container holding the water, and a window at the bottom allowed the water-filled membrane to contact the surface of the animal. Acoustic coupling gel or simply a thin layer of water was used to improve the acoustic coupling between the animal and the water-filled membrane. During imaging the nude mouse was anesthetized using a gas anesthesia machine (EZ-5000, Euthanex Corp., Palmer, PA) with 1 – 2% vaporized isofluorane at an air flow-rate of 1 – 1.5 L/min. Absorbing structures were detected above the noise floor to depths of 2.5 – 3 mm *in vivo*, as shown in Figure 2.8.

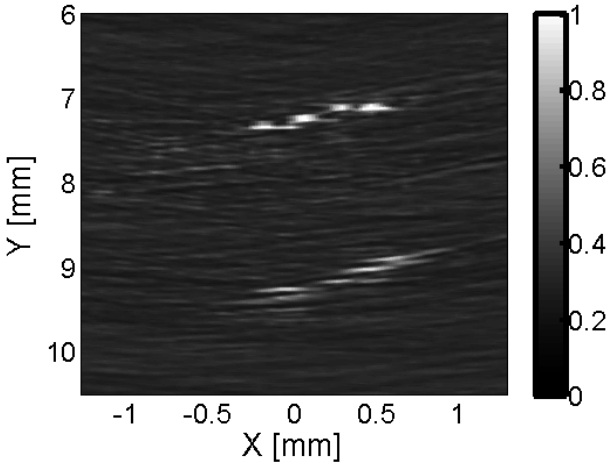

Figure 2.8. Photoacoustic image of microvasculature in a nude mouse. This figure demonstrates appreciable signal to depths of ~2.5 mm.

2.2.5 *In vivo* static and dynamic imaging

The multimedia file of Fig shows a movie of microvascular structures, where the subject and transducer are fixed relative to each other. Electronic noise generates a visible flicker in the

images, but because the system is real-time, the eye tends to provide a good temporal filter to distinguish static structures from random noise. The movie linked to Fig shows a 2-way fly-through of microvessels, where the array is translated over 10 – 15 mm along the array's elevation direction forwards then backwards. Notice the prominent oblique vessel structure which seems to be moving across the bottom of the field of view.

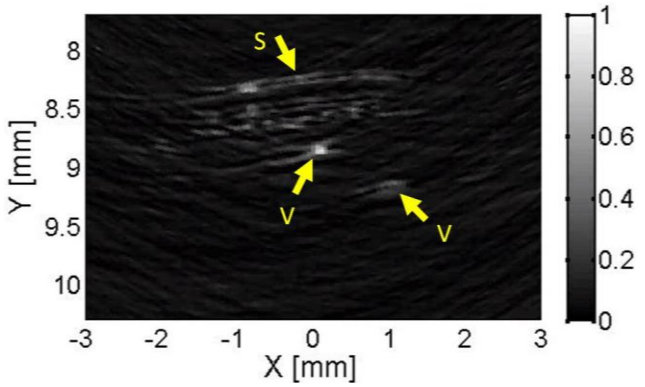

Figure 2.9. (3.2 MB) Photoacoustic movie sequence of subcutaneous microvasculature as the subject and probe are held in a fixed position. S is the skin surface and bright regions below the skin surface are microvessels including venules and arterioles. Two sample vessels are labeled with the letter V in the figure.

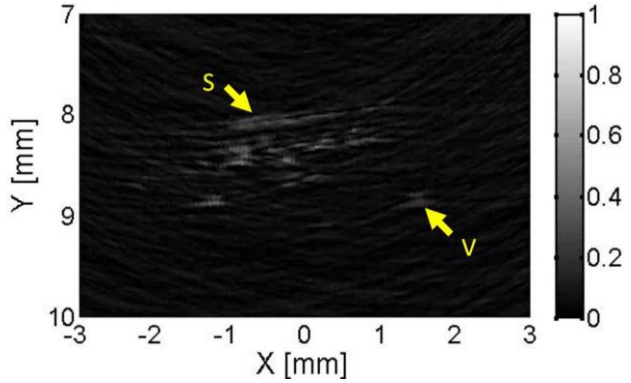

Figure 2.10. (4MB) Photoacoustic movie sequence of a 2-way fly-through across 10-15 mm over the skin surface S. Notice the prominent oblique vessel V move from the middle right to the center of the image and back as the array is translated along its elevation direction.

2.3 Discussion

The system presented here represents the first real-time high-frequency photoacoustic imaging system to our knowledge, and we have seen a glimpse of its capabilities. There is considerable room for forward progress and we now offer a discussion of such avenues.

Thus far, we have performed only single wavelength imaging. Future work may incorporate multiple-wavelength illumination for spectral estimation of blood oxygen saturation and other physiological parameters of interest. A fast-tuning laser source would be highly desirable for this application.

Presently the light delivery approach is not amenable to direct probe-skin contact and the transducer must be held above the skin surface. Future improvements should integrate a standoff mechanism to better control light delivery and facilitate contact measurements as this adds to handheld stability.

For exposure times longer than 10 s, the ANSI recommended limit for skin illumination is 200 mW/cm^2, a number designed to limit cumulative laser-induced heating. For <10 s dwell times, the maximum permissible exposure is limited by $1100t_e^{1/4}$ in mJ /cm^2, where t_e denotes the exposure duration in seconds. For our case, since we send a rapid train of 6 pulses followed by an inter-frame delay which is long enough for heat to adequately dissipate (as note above for 50 fps rates), we take the exposure duration as 6 ms. This corresponds to a total of 54.4 mJ/cm^2 delivered over the 6 pulses, translating into ~9 mJ/cm^2 per pulse, which is roughly our present fluence, even though our average power delivery is ~3 W/cm^2, above the CW ANSI limit. Higher imaging frame rates may induce undesirable laser-heating.

Heating can be minimized in future systems incorporating more digitization channels since the requirement for multiplexing is reduced. More acquisition channels will also reduce possible

motion artifacts for very fast motions, and allow for increased energy fluence per laser pulse, which will improve the signal-to-noise ratio and penetration depth. For significant penetration depths, a broader surface illumination may be advantageous as this will enable more multiply-scattered photons to be delivered to a given depth.

A broader illumination pattern will also increase our field of view. Presently our field of view with any appreciable signal-to-noise ratio is limited to ~3 – 4 mm axially and laterally. This is largely due to light delivery and penetration. Note however, that since our array transducer possesses 2λ pitch, grating lobes may be problematic for large steering angles. Thus, to increase the field of view we should also use a transducer with smaller pitch (although such transducers are presently difficult to fabricate), and more elements.

Future system designs should also take great care to design the RF electronics to reduce noise as much as possible—to approach the theoretical best-case Johnson (thermal) noise floor.

Finally, it is presently difficult to interpret our B-scan images without some reference image of the anatomical context. For this reason it would be greatly advantageous to integrate high-frequency pulse-echo ultrasound imaging capabilities in the system.

2.4 Conclusions

We have presented a first-of-its kind real-time high-frequency photoacoustic imaging system, have outlined our design including the hardware and software architecture, and have shown phantom and *in vivo* data. The B-scan acquisition rate is 50 frames/s, faster than the 30-Hz video rate. Also noteworthy is that this is the first article to our knowledge documenting real-time beamforming on a multi-core CPU desktop PC with high-level software, although others have certainly moved towards programmable hardware at a lower-level [51]. Because of the recent trend to multi-core processors, and leveraging Moore's Law, we may expect that our multi-

threaded software approach may have considerable potential for photoacoustic systems, ultrasound systems, and other multi-channel systems requiring beamforming as the number of processor cores expands. Having provided some discussion on the capabilities and limitations of our real-time photoacoustic imaging system, one question that remains to be seen is what biomedical applications can best make use of this emerging technology. With recent progress, real-time photoacoustic imaging is sure to find a niche in several biomedical applications. Now equipped with real-time imaging capabilities, photoacoustic imaging is ready to make seminal contributions in biological and clinical imaging.

Chapter 3 Real-time Photoacoustic Microscopy of Murine Cardiovascular Dynamics†

3.1 Introduction

Due to the rapid heart rates of mice, cardiovascular research utilizing murine models of disease requires high frame-rate imaging modalities. Presently, widely used small animal imaging techniques such as micro-PET and micro-CT do not permit imaging frame rates sufficient for murine cardiovascular visualization. High-frequency ultrasound has emerged as a valuable tool for cardiovascular research, offering both high resolution and high frame rates [52]. Beyond tissue structure and morphology, imaging systems offering functional imaging capabilities are highly desirable for cardiovascular research. Of particular interest is measurement of blood flow, which high-frequency ultrasound can provide, and estimation of local blood or tissue oxygenation, which ultrasound alone cannot. However, an emerging bio-imaging technology, photoacoustic imaging, has the potential for noninvasive oxygenation mapping [1]. This letter describes a unique real-time photoacoustic imaging system and its application in imaging the beating hearts of young athymic nude mice *in vivo*.

Photoacoustic imaging uses laser-induced ultrasound to form images of optical pigmentation in subcutaneous tissue. Photoacoustic signal strength is proportional to the local optical absorption coefficient of tissue, and scales in magnitude with the optical fluence delivered. Dominant subcutaneous absorbing pigments include oxy-hemoglobin and deoxy-hemoglobin, hence high contrast images of blood vessels and microvessels are possible [44]. With multiple optical wavelengths sequentially used to interrogate tissue, algorithms akin to those

† Reused with permission from [R. J. Zemp, L. Song]*, R. Bitton, K. K. Shung, and L. V. Wang, "Realtime photoacoustic microscopy of murine cardiovascular dynamics," *Optics Express* 16, 18551 (2008) (*equal contribution).

used in pulse-oximeters may be used to estimate blood oxygen saturation [36]. Additionally, photoacoustic technologies have been shown to be promising for molecular imaging, including gene expression imaging [53].

Recently, our group demonstrated a novel real-time photoacoustic imaging system based on a high-repetition-rate laser and a high-frequency ultrasound array transducer [26, 54]. In this letter, we report on the refinement of this system and its use for imaging in real-time the beating hearts of mice. To our knowledge, along with our recent conference paper, this is the first published report of real-time photoacoustic imaging of physiological dynamics.

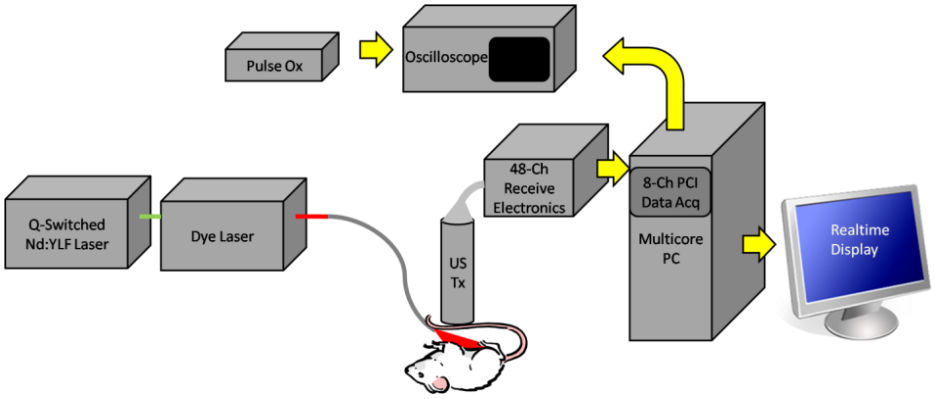

Figure 3.1. Diagram of our photoacoustic imaging system. A tunable pulsed laser system delivers light via an optical fiber to the animal subject. A high frequency ultrasound array transducer (US Tx) receives the photoacoustic signals, which are amplified and de-multiplexed using custom receive electronics, then digitized using an 8-channel PCI data acquisition card. A computer with 8 processor cores performs real-time beamforming and display. A pulse oximeter (Pulse Ox) was used to monitor animal health and measure animal heart rates.

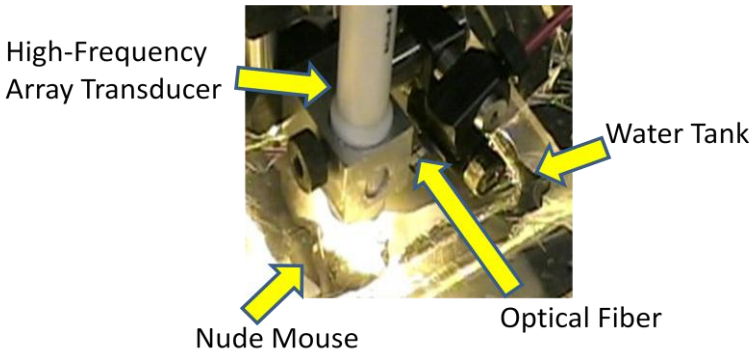

Figure 3.2. (1.8 MB) Video of the real-time photoacoustic imaging system and real-time display while imaging the beating heart of an athymic nude mouse.

3.2 Methods

Our system design is described in detail in [54], however we report the most salient features here, highlighting our current experimental protocol. An Nd:YLF Q-switched laser delivering 523-nm light pulses of 6 – 8-ns duration at up to 12-mJ pulse energy, and up to 1-KHz repetition rates was used to pump a tunable dye laser circulating Rhodamine 6G laser dye. The tunable laser output was fiber-coupled into a 600-μm high-numerical aperture optical fiber, and the light at the other end of the fiber was directed obliquely onto the imaging subject, forming an elliptical illumination pattern with ~10 mJ/cm^2 incident laser fluence. A custom high-frequency ultrasound array transducer (fabricated in the NIH Transducer Resource Group [46]), was used to receive high-frequency photoacoustic signals. The array possessed 48 elements with 30-MHz center frequency, 2-λ pitch, and 8.2-mm elevational focus. Custom receive and control electronics were used to amplify and multiplex received acquisitions, and an 8-channel PCI digitizer with 125 MS/s parallel digitization rate was used to acquire, digitize, and stream received photoacoustic signal data to the RAM of a dual-socket quad-core PC (possessing 8 processor cores). Real-time delay-and-sum beamforming was implemented using parallel programming on these processor cores, while scan conversion was offloaded to the Graphical

Processing Unit of the video card. The PCI digitizer served as master clock, and generated 6 trigger-out signals at 1 KHz repetition rate to the laser to acquire 48-channels of data using 6 multiplexed acquisitions. One multiplexed acquisition of the 48-channels was then used to form a single B-scan image frame, and inter-frame triggering was software generated, averaging ~50 frames per second. The system resolution was quantified as ~100 μm laterally, and 25 μm axially.

In this paper the laser trigger-signal from the PCI digitizer was also routed through a pulse-delay generator to an oscilloscope. Simultaneously another channel of the oscilloscope was used to record pulse-oximeter signals. The pulse-delay generator output a TTL pulse 7 ms in duration for the first trigger pulse it encountered, so that the train of 6 trigger pulses was effectively converted to a single TTL pulse for each image frame. The oscilloscope was hence used to record the occurrence of image frames relative to the cardiac cycle to validate that we were indeed imaging the heart in real-time, and not temporally under-sampling.

Young athymic nude mice (10 g) were purchased from Charles River Laboratories. Nude mice were anesthetized using a gas anesthesia machine according to approved protocols, and maintained under anesthesia using this machine throughout the imaging procedure. A pulse-oximeter probe was clamped to a hind-paw, and the animal was positioned so that its chest wall was facing the ultrasound transducer. The mouse was laid on a lab-jack with a soft plastic insulating bed. Fore- and hind-paws were secured to the lab-jack with adhesive tape. A thin layer of acoustic coupling gel was applied to the mouse, then the lab-jack and animal were raised up to an optically-and acoustically transparent water-filled membrane (Saran Premium Wrap™, SC Johnson Inc.) sagging from an aperture in a water tank. The purpose of this water tank was to serve as an acoustic coupling mechanism for photoacoustic signals, and as an optically transparent medium for light delivery. The photoacoustic probe, consisting of the

optical fiber and ultrasound array transducer were lowered into the water tank, and positioned with the aid of a 3-axis translation stage. Real-time display from our imaging system was also invaluable for probe positioning. Following animal positioning, computer-console control of the imaging system was used to initiate data recording. In deep anesthesia, animal heart rates recorded by the pulse-oximeter and oscilloscope averaged 180 – 240 beats per minute or 3 – 4 beats per second. The real-time imaging speed with real-time data archival to the hard-drive could be performed at rates as high as 50 frames per second, adequate for capturing several image frames per cardiac cycle.

3.3 Results

Figure 3.2 shows a video of the imaging system and real-time display, demonstrating visualization of the beating heart. Figure 3.3 shows a movie of the beating heart of the same mouse, while rendered offline. Figure 3.4 shows an M-mode image, consisting of A-scan lines from the midpoint of Figure 3.3 as a sequence of time. The motion of an absorbing structure is apparent as a periodic motion. Two gaps in the cardiac cycle are evident and attributed to respiratory-induced motion. Structures are visualized to depths of ~3 – 4 mm, roughly 1/3 of the estimated body thickness during the imaging procedure. The B-scan photoacoustic images shown here offer visualization of optically absorbing structures, and their motion with cardiac and respiratory cycles is evident. The images shown here were acquired with a single optical wavelength of 578-nm, an isosbestic point (i.e. a point where deoxy- and oxy-hemoglobin molar extinction coefficient are equal). With this wavelength, oxygenated blood is visualized with the same contrast as deoxygenated blood.

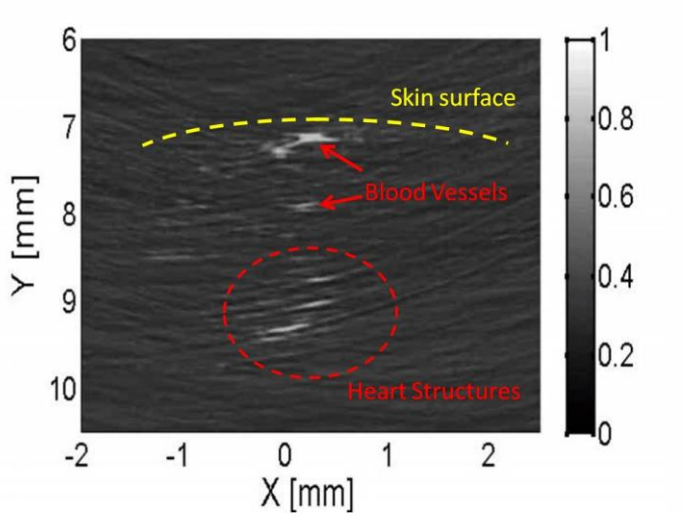

Figure 3.3. (3 MB) Photoacoustic B-scan movie of the beating heart of an athymic nude mouse. This movie sequence was reconstructed and rendered offline using data archived in real-time.

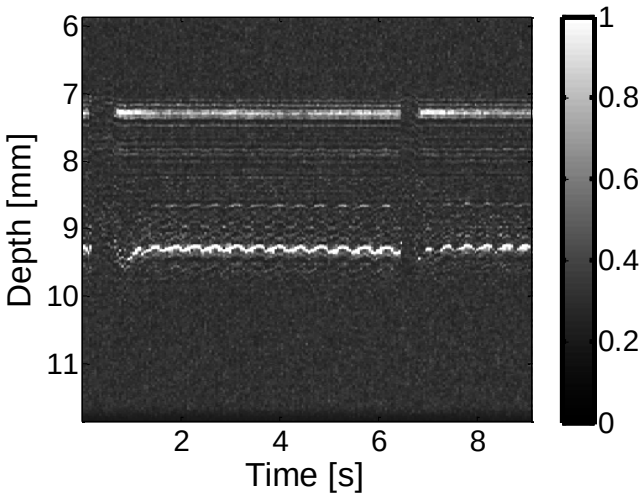

Figure 3.4. M-mode image along the *X* = 0 mm line in Figure 3.3. The oscillating structures around the 9-mm depth below the transducer surface show the cardiac motion as a function of time. The animal's heart estimated here as ~3 beats per second corresponded well to the 180 beats per minute as measured by the pulse oximeter.

3.4 Discussion

Presently, delineation of cardiac structures is difficult; however, complementary co-registered high-frequency ultrasound may serve this role in future work. Nevertheless, our system offers optical absorption contrast rather than ultrasound backscatter contrast, and these preliminary image sequences are the first of their kind. Image quality is expected to improve with future system improvements.

Active adult mice may have heart-rates from 400 to as high as 800 beats per minute (bpm) which may challenge our present 50 fps system. However, it is known that very young mice such as those used in our study, have lower heart-rates (286 +/- 56 bpm for newborns [55]). Additionally, anesthetized mice may have lower heart rates (anesthetic-dependent rates as low as 200 beats per minute for adult mice are reported in [56]). Hence the observed heart-rates are roughly consistent with the literature. In other data not shown we are able to image 300 bpm heart-rates. Deep breaths apparent in the movie and the M-mode data may suggest that improvements in animal positioning techniques are warranted.

Of considerable interest is the noticeable change in visibility of vessels during respiration, and may be due to venule expansion during respiratory-induced intra-thoracic pressure changes. This effect is worthy of further future study, and may prove important for studying venous return and diastolic function. These observations also motivate photoacoustic technology as a candidate for functional imaging studies, where a stimulus induces local vasoconstriction or vasodilation. Future work should also use multiple wavelengths for blood oxygenation estimation. This capability will prove important for studying ischemia in cardiovascular disease. Distinct from perfusion, oxygen saturation of tissues will provide important information linking tissue behavior to oxidative stress. Oxygen saturation may also be important for studying

developmental causes, consequences, and solutions to septal defects where oxygenated and deoxygenated blood mix during cardiac cycles. With future improvements, photoacoustic imaging technology may also help us understand hemodynamics in small animals with information which ultrasound alone cannot provide. Beyond small animal cardiovascular research, real-time photoacoustic imaging may serve an important future role in clinical settings, and we anticipate a bright future for this emerging technology.

Chapter 4 Fast 3D Dark-field Photoacoustic Microscopy *In vivo*[†]

4.1 Introduction

Photoacoustic imaging is a hybrid imaging modality with excellent optical absorption contrast and high resolution beyond the optical ballistic and quasiballistic regimes (~1 mm in scattering biological tissues) [20]. It has become a rapidly growing field in biomedical research because of its great potential in breast cancer diagnosis [57], skin melanoma detection [58], and functional brain imaging [34]. High imaging speed is essential for biomedical research involving dynamics and is highly desirable for decision-making in clinics. However, photoacoustic imaging systems using a single element ultrasound transducer are limited in speed by mechanical scanning. To improve imaging speed, several groups have employed ultrasound arrays for photoacoustic imaging [39, 59]. For example, using a 7.5 MHz ultrasound array, Niederhauser et al. [39] obtained an imaging speed of 7.5 B-scan-frames/s with 0.3 – 0.4 mm resolution. While ultrasound arrays of clinical diagnostic ultrasound frequencies (several MHz) are commercially available, arrays of high frequencies (>12 MHz) are still at the research stage. We developed a photoacoustic microscopy system with a high frequency (30 MHz) ultrasound array [26], which provided ~25 μm axial and <100 μm lateral resolutions. Real-time B-scan imaging capability was demonstrated [54].

Besides high imaging speed, 3D imaging is also highly desirable. One advantage of 3D imaging is to provide maximum amplitude projection (MAP) images in various orientations. Another advantage is the ability to view images interactively. The flexibility to rotate, scale, and view the region of interest from various perspectives can facilitate visualization.

[†] Reused with permission from L. Song, K. Maslov, R. Bitton, K. K. Shung, and L. V. Wang, "Fast 3-D dark-field reflection-mode photoacoustic microscopy *in vivo* with a 30-MHz ultrasound linear array," *Journal of Biomedical Optics* **13**, 054028 (2008).

We present a fast 3D dark-field reflection-mode photoacoustic microscopy system with a 30-MHz ultrasound linear array. This system performs real-time cross-sectional (B-scan) imaging at 50 Hz (faster than the 30-Hz video rate) with real-time beamforming and 3D imaging of 166 B-scan frames at 1 Hz with post-beamforming. To enable dark-field reflection-mode photoacoustic imaging, we designed a novel light delivery system consisting of both fiber and free-space optic components. The dark-field laser pulse illumination configuration was known to have advantages in suppressing undesirable photoacoustic signals from the superficial layers of the skin. Three-dimensional photoacoustic images of the subcutaneous vasculature in rats were demonstrated *in vivo*, which matched well with their *ex vivo* transmission optical microscopy counterparts. Our photoacoustic microscopy system is also presented as a compact prototype for handheld operation and is anticipated to accelerate preclinical and clinical applications of photoacoustic imaging.

4.2 Methods

A schematic of the system is shown in Figure 4.1. Our system consists of a diode-pumped Q-switched Nd:YLF laser, a tunable dye laser, a 30-MHz ultrasound linear array, custom receive and control electronics, an 8-channel PCI data acquisition (DAQ) card, a multi-core PC, a custom designed light delivery system, and a motorized linear motion actuator.

4.2.1 Optics and light delivery

As the irradiation source, the tunable dye laser (Cobra, Sirah Laser-und Plasmatechnik GmbH, Germany) was pumped by the Nd:YLF laser (INNOSLAB, Edgewave GmbH, Germany). The Nd:YLF pump laser had a pulse duration of 7 ns and a pulse energy of 12 mJ at 523 nm. The continuous optical pumping from the diode stacks in this Q-switched Nd:YLF laser provided the flexibility of

external triggering on demand at rates up to 1 kHz without compromising the pulse energy. This feature offered a significant advantage over flashlamp-pumped Q-switched lasers, which are

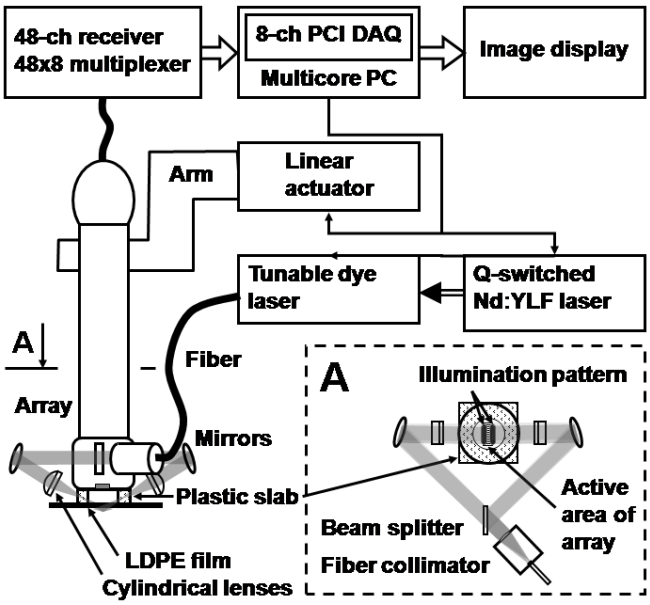

Figure 4.1. Schematic of the 3D dark-field reflection-mode photoacoustic imaging system.

typically maintained at a fixed low pulse repetition rate (e.g., 10 Hz). Rhodamine 6G laser dye was used to enable a peak output of 2 mJ per pulse with a pulse width of 7 ns at the 570-nm wavelength from the dye laser, with a 40-nm tuning range. For our imaging experiments, we used the peak 570-nm wavelength. This wavelength also corresponds to an isosbestic point where oxy- and deoxy-hemoglobin have equal molar extinction coefficients.

Proper delivery of laser light into biological tissues for photoacoustic excitation is crucial to achieving a high signal-to-noise ratio (SNR) in photoacoustic imaging. The light delivery system was designed to provide a compact photoacoustic imaging device with sufficient SNR and robust performance. The dye laser output was coupled into a 0.6-mm-core-diameter multimode optical fiber, and was collimated by a fiber collimator at the output end of the fiber. A free space optic

setup, integrated with the ultrasound array, was used to guide light further (Figure 4.1). The collimated light beam, of ~6 mm diameter and ~1.2 mJ energy, was split into two beams by a 50:50 non-polarizing beamsplitter. The two beams were reflected by mirrors towards two cylindrical lenses and were coupled into a plastic slab. The 6-mm thick plastic slab, with a hollow cylindrical core for the ultrasound probe, was polished for light transmission. During experiments, the cylindrical space was filled with water and sealed by a piece of thin low-density polyethylene (LDPE) film fixed by an o-ring. In total, ~80% of the light energy reached the surface of the film. Due to finite fiber aperture the final optical illumination patterns on the skin surface were thick-line shaped, as shown in Figure 4.1. The length and width of each illumination area were 6 and 3 mm, respectively.

Dark-field laser pulse illumination was achieved through fine tuning the mirrors and cylindrical lenses, reducing the photoacoustic signals from the superficial paraxial area. However, a large dark-field area may reduce the optical fluence reaching the targeted area. The optimal illumination radius was estimated to be 7 mm using the concept of effective attenuation coefficient [60], the exponential decay rate of fluence far from the source, with typical tissue parameters. Consequently, leaving a ~1 mm width right below the array elements as the dark field gives approximately the best performance. In practice, the mirrors and cylindrical lenses were finely tuned to optimize the SNR.

The optical fluence on the skin surface was estimated to be ~2 mJ/cm^2 per pulse, well below the ANSI recommended Maximum Permissible Exposure (MPE) of 20 mJ/cm^2 for a single pulse. We acquired data in 1 s—50 frames for real-time B-scan imaging or 166 frames for 3D imaging; the time average light intensity during this 1 s was ~600 mW/cm^2 (the total illuminated surface area for one 3D image was 1.2 cm^2 due to the mechanical scanning), also below the ANSI

recommended MPE calculated as $1.1t^{0.25}$ W/cm^2 (t in sec.) [61]. For prolonged illumination, the ANSI recommended MPE for average light intensity would be lower. However, for prolonged illumination during B-scan imaging, we can either pause a few seconds between acquisitions or slow down the frame rate. We also expect to reduce the delivered energy with improved SNR by system optimization. The ANSI safety limit for this pulse width region is dominantly based on the thermal mechanism; thus our compliance to the ANSI standards guarantees no thermal damage to the tissue.

4.2.2 Ultrasound array and beamforming

We used a unique 30-MHz ultrasound linear array fabricated from a 2-2-piezo-composite by the NIH Resource Center for Medical Ultrasonic Transducer Technology at the University of Southern California [46]. The array had 48 elements (of dimensions 82 μm × 2 mm) with 100-μm spacing. The dimension of the element in the elevation direction was 2 mm, and the elements were focused in this direction with a fixed focal length of 8.2 mm, which provides a resolution of ~300 μm in the elevation direction within the ~3.5 mm focal zone. The pulse-echo insertion loss and element cross-talk were 19.1 and -25 dB, respectively. The mean fractional bandwidth was 50% for pulse-echo operation, which translates to ~70% for receiving-only operation, as used in our present photoacoustic imaging system.

While ultrasound beamforming traditionally has used dedicated hardware [62], we instead used multi-core processors (Dell Precision 490 with two 2.66 GHz Quad core Xeon processors), which allows off-the-shelf personal computers to perform the task and offers programming flexibility. Microsoft Visual Studio 2005 Professional Edition and Microsoft XNA Game Studio in the Visual Studio C# 2005 Express Edition environment were used to develop the software for dynamic receive beamforming and display. Details on implementation of multi-threaded parallel

programming and GPU-based scan conversion and display in this software beamforming can be found elsewhere [54].

4.2.3 Data acquisition and volume imaging

Photoacoustic signals picked up by the ultrasound array were amplified by a custom-built RF board with a 33–73 dB variable gain and were down-multiplexed to eight channels, which were digitized at 125 mega-samples per second (MSPS) using a 14-bit 8-channel PCI DAQ card (Octopus CompuScope 8389, GaGe Applied Systems, USA). The card was used as the master clock for the entire system and was programmed to send trigger signals to the multiplexer control and laser. The repetition rate was set at 1 kHz, which was the highest rate that the laser could work without degradation of pulse energy.

We used linear scanning to achieve 3D imaging. During the scanning, the array translated linearly over the skin surface, so that the B-scan imaging planes were all parallel to each other. This was accomplished by mounting the light delivery system and the ultrasound array in a linear motion actuator (KR20, THK CO. LTD., Japan). A bipolar stepper motor (4118S, Lin Engineering, USA) controlled by a microstep stepper motor controller (BC2D15, Peter Norberg Consulting, Inc., USA) was used to drive the linear motion actuator. The scanning system provided sufficient precision (20 μm) for our use. Six laser shots were needed to obtain one B-scan image because of the 6:1 down-multiplexing in our data acquisition. To produce one 3D image, 166 B-scan frames were acquired in 996 ms, corresponding to 996 laser shots at a 1-kHz repetition rate. During the data acquisition, the array scanned continuously at a constant speed (10 mm/s). The speed was set so that the distance the array travelled during each B-scan time period was 60 μm, less than the ultrasonic focus in the elevational direction (~300 μm). Although the linear motion actuator was fixed on an optical table for scanning, handheld

operation was also possible. More user-friendly handheld operation for daily clinical use can be achieved by shrinking the size of the light delivery and scanning systems through custom manufacturing.

While real-time B-scan imaging was demonstrated at 50 frames per second (FPS), post-beamforming after data acquisition reached 83 FPS. This higher speed was due to less hardware communication. In post-beamforming, a B-scan movie was first played, and an MAP of the acquired 3D image was then displayed for preview immediately. In total, ~3 s was needed for a user to view an MAP image, representing the fastest speed among reported photoacoustic imaging systems. The user might choose to either replay the B-scan movie or display a contrast-enhanced MAP image processed by a Dynamic-link Library (DLL) written in MATLAB (Math Works, Inc., USA). All these operations could be done online by simply clicking corresponding buttons on a graphic user interface (GUI) generated by the C# program.

4.3 Results

The spatial resolution of our system was characterized by imaging 6-μm-diameter carbon fibers in water. The axial, lateral, and elevational resolutions (at ~7 mm normal depth from the transducer surface) were estimated to be 25, 70, and ~300 μm, respectively. The imaging depth was demonstrated to be greater than 3 mm in scattering biological tissues.

To demonstrate the system's capability to image blood vessels *in vivo*, we imaged the upper dorsal region of a Sprague Dawley rat (Harlan Sprague Dawley, Inc., USA), ~95 g in weight. The rat was anesthetized by intramuscular injection of a mixture of Ketamine (85 mg/kg) and Xylazine (15 mg/kg). The hair in the imaged region was removed with commercial hair-removal lotion before imaging. Acoustic coupling gel was applied to improve acoustic coupling between the animal and the LDPE film. After the experiment, the rat recovered normally, without

noticeable health problems. All experimental animal procedures were carried out in compliance with approved protocols.

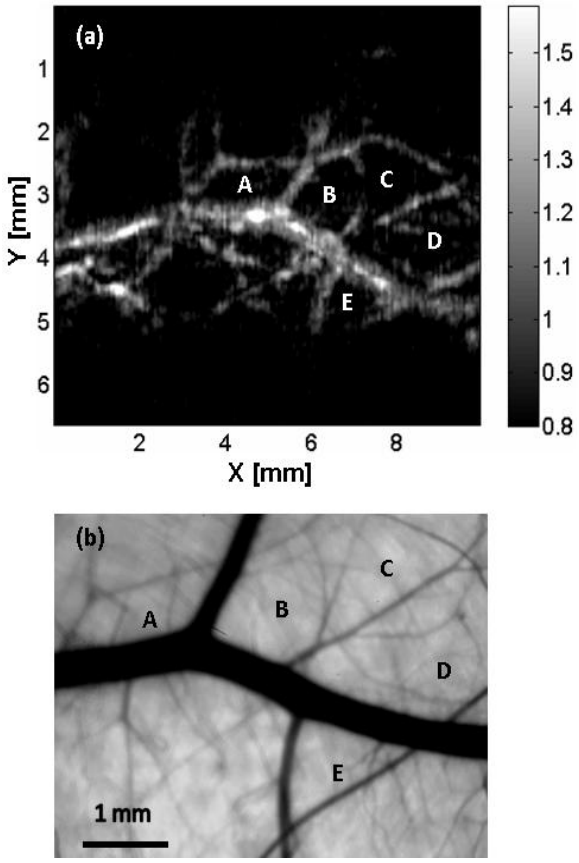

Figure 4.2. (a) *In vivo* noninvasive maximum amplitude projection photoacoustic image of subcutaneous blood vessels in the upper dorsal region of a Sprague Dawley rat. X and Y represent the mechanical scan and electronic beamforming directions, respectively. The grayscale represents relative optical absorption (arbitrary unit). The regions enclosed by major blood vessels are labeled using capital letters A–E. (b) Photograph taken from the dermal side of the excised skin with transmission illumination. The same regions are identified and labeled A–E. The photograph covers most of the photoacoustically imaged region.

Figure 4.2 shows an *in vivo* MAP photoacoustic image and an *ex vivo* transmission optical microscopic image of the subcutaneous vasculature in an imaged area. The photoacoustic image is a gray-level plot of the maximum amplitude of the envelope of each time-resolved (A-scan) photoacoustic signal within a 2 mm depth from the skin. The signals from the skin surface were digitally removed. The transmission optical microscopic photograph (~4 × 5 mm), partially overlapping with the photoacoustic image, was acquired *ex vivo* from the dermal side of the excised skin. As shown in Figure 4.2, the vascular distributions matched well between the two images. Vessels shown in the photoacoustic image had diameters varying from ~80 to ~700 μm. The data acquisition of the photoacoustic image was completed within 1 s, and the MAP image was displayed within 3 – 4 s. An animation of the 3D image from varying perspectives (Figure 4.3) was obtained from post-processing using VolView (Kitware Inc., USA). Interactive features (rotation, scaling, etc.) were available in VolView as well.

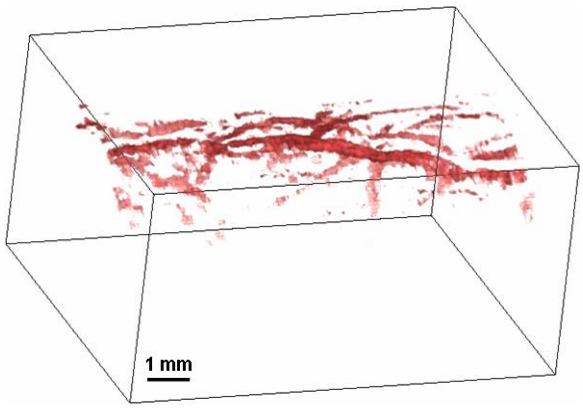

Figure 4.3. Movie of *in vivo* three-dimensional photoacoustic images of the upper dorsal region of a Sprague Dawley rat [Video 1].

To validate the system's reproducibility, we imaged a sacrificed Sprague Dawley rat noninvasively *in situ*. The experimental procedures were similar to those described above, except that the rat was sacrificed to avoid imaging artifacts due to breathing motion. We repeated scanning the same area (in the lower dorsal region) four times, with a time interval of ~2 min. The system demonstrated robust performance, with major vessels shown consistently in all four images (Figure 4.4).

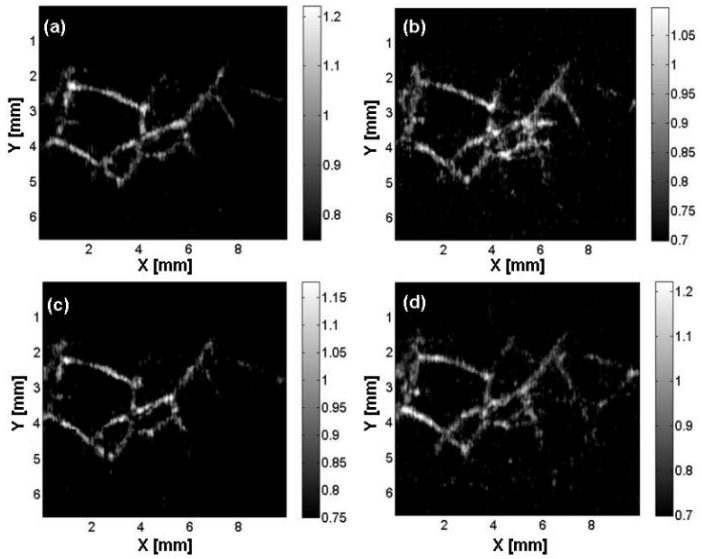

Figure 4.4. Four consecutive photoacoustic-image acquisitions of the same lower dorsal area of a sacrificed Sprague Dawley rat (images were acquired noninvasively *in situ*). The grayscale represents relative optical absorption (arbitrary unit). The major vessels are shown consistently.

4.4 Discussion and conclusions

We have demonstrated fast 3D photoacoustic microscopy with a 30-MHz ultrasound linear array capable of real-time B-scan imaging at 50 Hz and 3D imaging at 1 Hz. To our knowledge, this is the fastest photoacoustic imaging achieved hitherto. The system integrates a novel light delivery system and a motorized linear motion actuator with the ultrasound array, performing scans in elevational direction for 3D imaging. The light delivery system enables robust reflection-mode

imaging, which is applicable to more anatomical sites than orthogonal- or transmission-mode imaging. Optical dark-field illumination is also achieved, reducing the otherwise strong interference of the extraneous photoacoustic signals from the superficial paraxial area. The imaging performance is validated to be robust and reproducible.

Previous studies have demonstrated that photoacoustic imaging has great potential in early cancer diagnosis, blood oxygenation mapping, and functional brain imaging. Because of the unique real-time 2D and fast 3D imaging capability, our system is anticipated to facilitate many of these biomedical applications. The compact system design also favors clinical practices. Particularly, the promising results shown in this report should motivate future development of photoacoustic microscopy with high frequency ultrasound arrays towards clinical applications.

Chapter 5 High-speed Dynamic 3D Photoacoustic Imaging of Sentinel Lymph Nodes in a Murine Model[†]

5.1 Introduction

The sentinel lymph node (SLN) hypothesis, popularized by Morton et al. [63] and Giuliano et al. [64] in the early 1990s, states that it is sufficient to assess lymphatic metastasis by examining the first tumor-draining (sentinel) lymph node. Sentinel lymph node biopsy, based on this concept, has emerged as the standard of care in breast cancer [65]. In SLN biopsy, radioactive colloids (e.g., Tc-99m sulfur colloids) are injected preoperatively to locate the SLN with a handheld gamma probe, followed by a blue dye (e.g., methylene blue) injection to precisely locate it intraoperatively for dissection. SLN biopsy has greatly reduced unnecessary lymph node dissections and thus the risk of associated complications (e.g., lymphedema). However, it also has drawbacks:

- Up to 60 learning cases may be required to develop technical proficiency [66] (in published results without a high number of learning cases per surgeon, up to 16% of SLNs were missed [67]).
- The false negative rate is estimated to be ~5 – 10%, even in experienced hands [68, 69].
- The technique involves radioactive tracer, which requires a separate injection procedure and radiation safety protections.
- Although less invasive than axillary lymph node dissection, it still has associated morbidity such as seroma formation, lymphedema, and sensory nerve injury [70].

These drawbacks suggest that alternative strategies for SLN identification should be explored.

[†] Reused with permission from L. Song, C. Kim, K. Maslov, K. K. Shung, and L. V. Wang, "High-speed dynamic photoacoustic imaging of sentinel lymph node in a murine model using an ultrasound array," *Medical Physics* **36**, 3724 (2009).

Ultrasound-guided fine needle aspiration biopsy (FNAB) has been reported as a less invasive alternative to SLN biopsy [71, 72]. Unfortunately, although ultrasound can detect hypo-echoic lymph nodes, it cannot distinguish the sentinel node because blue dyes have little mechanical contrast. Near infrared (NIR) fluorescence imaging has been actively explored for SLN mapping [73-75]. This imaging technique performs real-time imaging capable of capturing the dynamics in SLNs [76]. However, due to the strong optical scattering in biological tissue, conventional fluorescence imaging has difficulty in identifying deep SLNs with high spatial resolution. Another challenge for fluorescence imaging is the relatively low quantum yield of clinically approved fluorophores (e.g., ICG) [74]; while quantum dots have high quantum yield, the issue of potential toxicity has to be addressed [77].

Photoacoustic imaging combines the advantages of excellent optical absorption contrast and high ultrasonic resolution at great depths, up to a few centimeters [78]. Our group recently demonstrated that photoacoustic imaging with methylene blue dye injection can accurately identify SLNs at depths up to 31 mm—greater than the mean SLN depth of 12 $\pm$ 5 mm in humans [79]—in scattering biological tissue in a rat model [80, 81]. Given the use of only conventional blue dye that is already part of the current standard of care, photoacoustic imaging is a promising technology for accurate SLN mapping, potentially capable of improving the false negative rate in SLN identification. With the demonstrated high spatial resolution, it may also have the potential to replace SLN biopsy with fine needle aspiration biopsy, and thus to reduce the risk of associated morbidity.

In photoacoustic imaging with a single-element ultrasonic transducer, the data acquisition speed is usually limited by the raster scanning [80, 81]. Fortunately, this drawback can be overcome by using an ultrasound array. With a high-frequency ultrasound array, we recently developed a

photoacoustic imaging system that performs 50 Hz real-time B-scan imaging and high-speed 3D imaging—one 3D image acquisition takes 1 s [82-84]. We believe that this imaging speed is highly desirable in clinics, and it is expected to facilitate the study of photoacoustic SLN mapping. In this study, we demonstrated the feasibility of SLN mapping in a murine model with our refined high-speed 3D photoacoustic imaging system. Evans blue, a blue dye used in clinical SLN biopsy [85, 86], was employed to provide the optical absorption contrast (with the peak absorption wavelength at ~620 nm, and the two half-maximum wavelengths at ~540 and 650 nm, respectively [87]) for photoacoustic imaging. In addition, the dye dynamics in SLNs were quantitatively monitored with a 3D imaging temporal resolution as high as ~6 s.

5.2 Materials and methods

5.2.1 Imaging system

Figure 5.1 shows a schematic of the high-speed 3D photoacoustic imaging system. While the laser and the imaging head were fixed on an optical table, all the electronics were placed on a movable rack, creating a system potentially transportable to the clinics.

For photoacoustic wave excitation, a tunable dye laser (Cobra, Sirah Laser-und Plasmatechnik GmbH, Germany), pumped by a Q-switched Nd:YLF laser (INNOSLAB, Edgewave GmbH, Germany), was used. The Q-switched laser could be externally triggered up to 1 kHz without compromising pulse energy, which, together with the use of an ultrasound array and a multi-core computer for parallel beamforming, was critical to achieve the high imaging speed. The Q-switched laser had a pulse duration of <10 ns and a pulse energy of 11 mJ/pulse at 523 nm. The dye laser, with Pyrromethene 597 dye, had a peak output at 582 nm and a tunable

range from 561 to 610 nm. The output energies from the dye laser at 584 and 600 nm—the two wavelengths used for the experiments—were ~2.5 and ~1.5 mJ/pulse, respectively.

The dye laser output was split into two beams and coupled into two 0.6-mm-core-diameter multimode optic fibers. The light beams from the output end of the optic fibers were cylindrically focused and delivered to the object to be imaged. As shown in Figure 5.1 (inset A), dark-field laser illumination was used to reduce the photoacoustic signals from the superficial paraxial area [88-91]. The optical fluence on the skin surface of the object was estimated to be ~0.5 – 1.0 mJ/cm^2 per pulse, well below the ANSI recommended Maximum Permissible Exposure (MPE) of 20 mJ/cm^2 for a single pulse. The time averaged light intensity during image acquisition was ~150 – 300 mW/cm^2, also below the ANSI recommended MPE calculated by $1.1t^{0.25}$ W/cm^2 (t in seconds) [92]. As the ANSI safety limit for this pulse width region is dominantly based on the thermal mechanism, our compliance with the ANSI standards guarantees no thermal damage to the tissue.

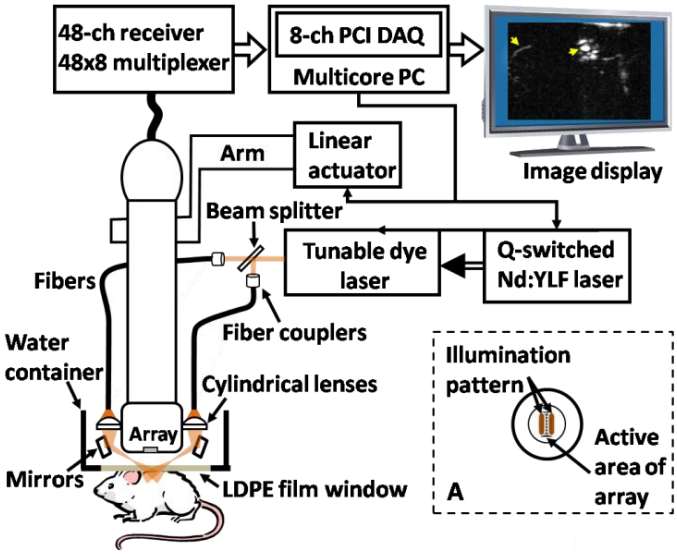

Figure 5.1. Schematic of the high-speed 3D photoacoustic imaging system. Inset A, optical illumination pattern on the skin surface.

We used a unique 30-MHz ultrasound array fabricated from a 2-2-piezo-composite by the NIH Resource Center for Medical Ultrasonic Transducer Technology at the University of Southern California. The array had 48 elements (82 μm × 2 mm) with 100 μm spacing. The elements were elevationally focused at 8.2 mm, providing an elevational resolution of 300 μm within the ~3.5 mm focal zone. The mean fractional bandwidth was 50% for pulse-echo operation, translating to ~70% for receiving-only operation, as used in our present photoacoustic imaging system. The axial and lateral resolutions of the system at 8 mm normal depth from the transducer surface were ~25 and ~70 μm, respectively.

While cross-sectional B-scan images were obtained by electronic beamforming using a multi-core PC (Dell Precision 490 with two 2.66 GHz Quad core Xeon processors), 3D photoacoustic images were acquired by linearly translating the array—using a linear motion actuator—in a water container (Figure 5.1). The water container, with dimensions of 8 cm × 5 cm × 3 cm, had a thin low-density polyethylene (LDPE) membrane window transparent to light and ultrasound. Acoustic gel was used for ultrasonic coupling between the membrane and the object. With this design, there was no direct contact between the moving imaging head and the object, minimizing potential perturbations produced by the mechanical scanning.

A high-speed (125 mega-samples per second) 14-bit 8-channel DAQ card (Octopus CompuScope 8389, GaGe Applied Systems, USA) was used for data acquisition. Because of the 6:1 down-multiplexing in data acquisition, six laser shots were needed to obtain one B-scan image. The card was used as the master clock for the entire system and was programmed to send trigger signals to the multiplexer control and laser. The repetition rate was set at 1 kHz, which was the highest rate that the laser could reach without degradation of pulse energy.

To obtain one 3D image, 166 B-scan frames were acquired in 996 ms, corresponding to 996 laser shots at a 1-kHz repetition rate. During the data acquisition, the array scanned at a constant speed of 10 mm/s. The speed was set so that the distance the array travelled during each B-scan was 60 μm, less than the 300 μm ultrasonic elevational focus. For sequential 3D image acquisition, the system has a temporal resolution of ~6 s, currently limited by the time for writing data to the hard drive and post-beamforming after each 3D data acquisition.

5.2.2 Animal model and *in vivo* imaging

Hsd:Athymic Nude mice (Harlan Laboratories, Inc., USA) weighing ~18 g and Sprague Dawley rats (Harlan Laboratories, Inc., USA) weighing ~120 g were used for the experiments. An intra-dermal injection of a mixture of ketamine (85 mg/kg) and xylazine (15 mg/kg) was used for initial anesthesia. For rats, the hair in the axillary region was removed with commercial hair-removal lotion before imaging. During all image acquisitions, anesthesia was maintained using vaporized isoflurane (Euthanex Co., USA). The animals were euthanized by pentobarbital overdose after experiments. All experimental animal procedures were carried out in compliance with Washington University approved protocols.

For each experiment, a control photoacoustic image of the region of interest was acquired before dye injection. Then *in situ* intra-dermal injection of Evans blue dye (Sigma-Aldrich Co., USA) was performed on the left forepaw pad. Photoacoustic imaging was started immediately after the dye injection. Thereafter, images were acquired every ~8 s for the initial few minutes; subsequent image acquisitions were done at longer intervals for a prolonged period, up to 1.5 hours. Two laser wavelengths were used for the experiments, 584 nm and 600 nm. The former is close to the peak-output wavelength of the dye laser, and was used to image the SLNs and blood vessels simultaneously—this wavelength also corresponds to an isosbestic point where

oxy- and deoxy-hemoglobin have the same optical absorption coefficient. The latter is close to the absorption peak of Evans blue, and was used to image primarily the SLNs. The goal was to noninvasively identify the SLNs accurately, and meanwhile capture the dye dynamics.

5.3 Results

A mouse SLN was imaged noninvasively *in vivo* using the high-speed photoacoustic imaging system. Figure 5.2(A) is a photograph of the mouse taken before photoacoustic imaging, showing the axillary region. The black tape in the photograph was used to guide the initial positioning of the imaging head. Figure 5.2(B) is a photoacoustic control image acquired at 600 nm, shown in the form of maximum amplitude projection (MAP), which was created by projecting the maximum photoacoustic amplitudes along the depth direction to the skin surface. A few blood vessels were imaged, but the images have low contrast because of the low energy output from the dye laser and the decreased hemoglobin absorption at this wavelength [93]. Figure 5.2(C) is a photoacoustic MAP image acquired at 600 nm ~8 s after injection of ~100 μg (1%, 0.01 ml) Evans blue. The SLN as well as an afferent lymph vessel are clearly seen. As 600 nm is close to the Evans blue peak absorption wavelength (620 nm), the SLN shows excellent contrast in the image. Figure 5.2(D) is a control photoacoustic image acquired at 584 nm, showing the subcutaneous vasculature. The spatial resolutions are 70 μm in the lateral (vertical) and 300 μm in the elevational (horizontal) directions, respectively. After Evans blue injection, both the vasculature and SLN were imaged (Figure 5.2(E)). A composite of the two photoacoustic MAP images acquired at 600 and 584 nm was obtained (Figure 5.2(F)). In this composite image, the blood vessels and dyed lymphatic system—the SLN and lymph vessel—are clearly seen, with high contrast and good resolution. The distance between the top surface of the SLN and the skin surface was estimated to be 650 ± 50 μm from the composite B-scan

image (Figure 5.2(G)). A composite 3D image, constructed with VolView (Kitware Inc., USA), is shown in Figure 5.2(H). An invasive photograph of the same mouse, with the skin removed, was taken after photoacoustic imaging (Figure 5.2(I)). The SLN was embedded in fatty tissue, and thus difficult for naked eyes to locate precisely, even with the skin removed. The dynamic behavior of Evans blue in the SLN is shown in Figure 5.3(G) (mouse 1), obtained with the aforementioned data acquisition strategy. Each data point in Figure 5.3(G) was computed as the photoacoustic signal averaged over the entire SLN area in the corresponding MAP image (normalized by the temporal maximum value of the same SLN). The data points were exponentially fitted to show the change more clearly. In this case, the photoacoustic signal was observed to decrease with time from the first recorded point (8 s), and was of ~10% peak value after ~1.5 hours.

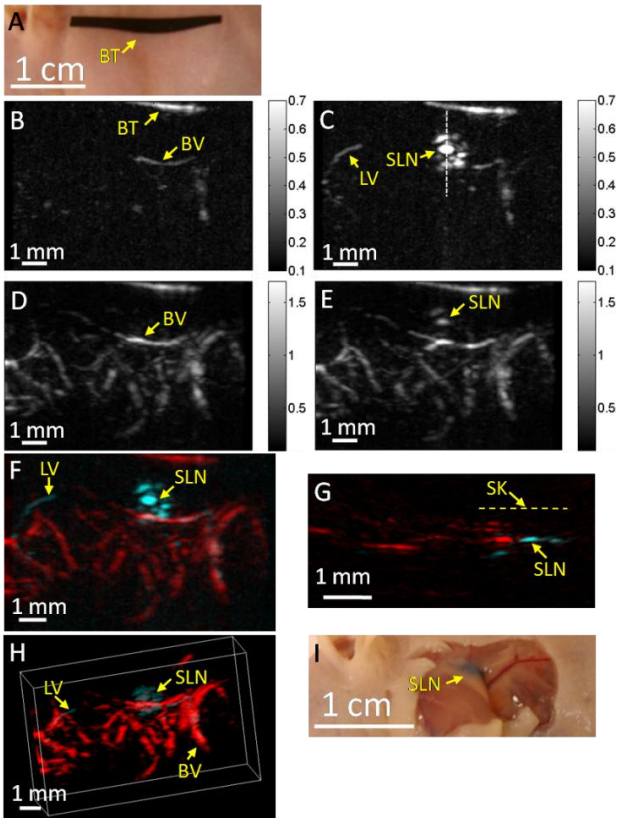

Figure 5.2. Noninvasive *in vivo* photoacoustic mapping of the sentinel lymph node in a mouse. (A) Photograph taken before photoacoustic imaging. BT, black tape, was used to guide the initial positioning. (B) Control photoacoustic MAP image acquired at 600 nm laser wavelength before Evans blue injection. BV, blood vessel. The colorbar represents optical absorption. (C) Photoacoustic MAP image acquired at 600 nm 8 s after Evans blue injection. SLN, sentinel lymph node. LV, lymph vessel. (D) Control photoacoustic MAP image acquired at 584 nm. (E) Photoacoustic MAP image acquired at 584 nm 8 min after Evans blue injection. (F) Composite photoacoustic MAP image. Blood vessels from the 584 nm image are pseudo-colored red and the sentinel lymph node and lymph vessel from the 600 nm image light blue. (G) Composite photoacoustic B-scan image corresponding to the dotted line in (C), showing the depth of the SLN. SK, skin surface. (H) Composite 3D photoacoustic image. (I) Photograph taken with skin removed after photoacoustic imaging.

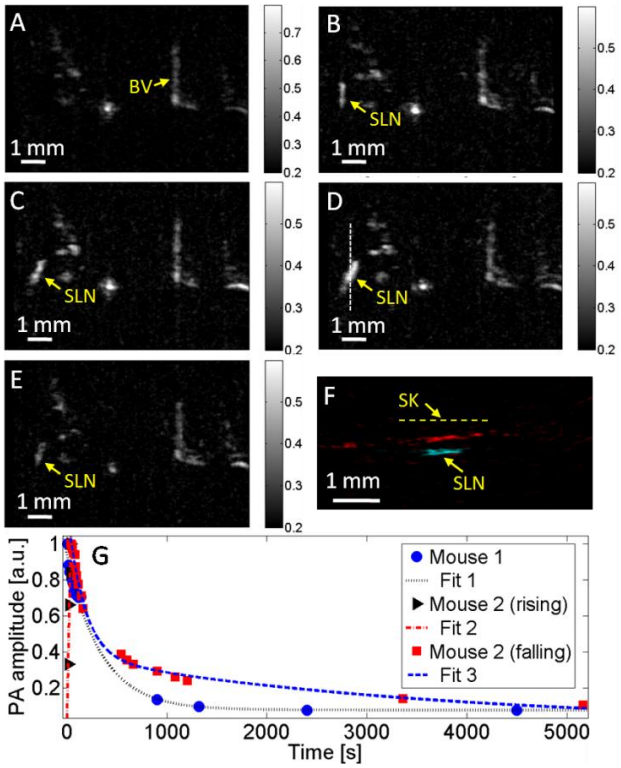

Figure 5.3. Evans blue dynamics in the sentinel lymph node (SLN) of a mouse monitored by photoacoustic imaging. (A) Control photoacoustic MAP image in a mouse (mouse 2) acquired before Evans blue injection. BV, blood vessel. The colorbar represents optical absorption. (B) – (E) Photoacoustic MAP images acquired at 14 s, 22 s, 38 s, and 20 min, respectively, after Evans blue injection. (F) Composite photoacoustic B-scan image corresponding to the dotted line in (D). SK, skin surface. Blood vessels from the 584 nm image are pseudo-colored red and the sentinel lymph node from the 600 nm image light blue. (G) Evans blue dynamics in mice SLNs. Data points were fitted exponentially. PA, photoacoustic.

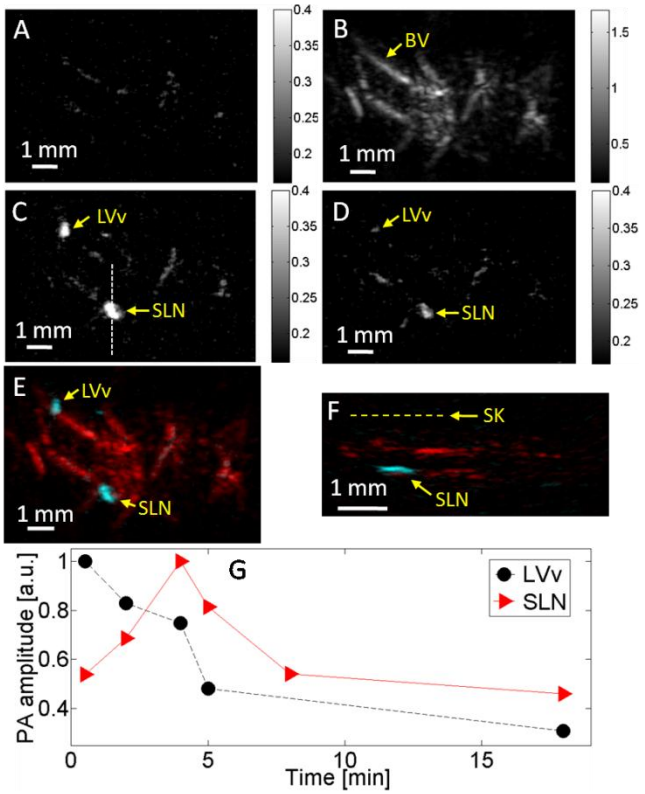

Figure 5.4. Noninvasive *in vivo* photoacoustic mapping and dynamic monitoring of the sentinel lymph node in a rat. (A) Control photoacoustic MAP image acquired at 600 nm laser wavelength before Evans blue injection. (B) Control photoacoustic MAP image acquired at 584 nm, showing the subcutaneous vasculature. (C) Photoacoustic MAP image acquired at 600 nm 6 min after Evans blue injection. LVv, lymphatic valve; SLN, sentinel lymph node. (D) Photoacoustic MAP image acquired at 600 nm 15 min after Evans blue injection. (E) Composite photoacoustic MAP image. Blood vessels from the 584 nm image are pseudo-colored red and the sentinel lymph node and lymphatic valve from the 600 nm image light blue. (F) Composite photoacoustic B-scan image corresponding to the dotted line in (C). SK, skin surface. (G) Evans blue dynamics in the rat lymphatic valve and SLN.

Another mouse was imaged with the same scheme, but with less Evans blue injection—~32 μg (0.4%, 0.008 ml). This time, a signal increase was observed within the initial ~40 s (Figure 5.3(A – D)), followed by a subsequent decrease (Figure 5.3(E)). A composite B-scan image (Figure 5.3(F)) along the dotted line in Figure 5.3(D) was obtained, showing the depth of the SLN. The quantitative dynamics were plotted in Figure 5.3(G) (mouse 2), showing both a rising and a falling phase.

A rat was also imaged. After taking the control images at 600 nm (Figure 5.4(A)) and 584 nm (Figure 5.4(B)), ~300 μg (1%, 0.03 ml) of Evans blue was injected. In this case, the SLN as well as a lymphatic valve were identified (Figure 5.4(C)). A photoacoustic image taken at 600nm 15 min after Evans blue injection showed a sharp signal decrease from the lymphatic valve, which became barely visible, while the SLN was still clearly imaged (Figure 5.4(D)). A composite image was formed to show the dyed lymphatic system and the blood vessels (Figure 5.4(E)). The composite B-scan image indicates that the SLN is at a depth of ~1.2 ± 0.1 mm below the skin surface (Figure 5.4(F)). The signal from the lymphatic valve decreased with time from the first recorded data, while the SLN exhibited both a rising phase and a falling phase, showing the dynamics of both dye accumulation and clearance (Figure 5.4(G)).

5.4 Discussion

Compared with pure optical imaging modalities, photoacoustic imaging is known to have high resolution at a greater imaging depth—beyond the ballistic and quasi-ballistic regime in scattering biological tissue—with excellent optical absorption contrast [22, 88]. It is also a high-speed imaging modality by nature, with the speed fundamentally limited by the time of arrival of the photoacoustic waves, which, for example, should allow A-line acquisitions at up to 100 kHz rate at a depth of 1.5 cm. Photoacoustic imaging using a 1-D ultrasound array eliminates

mechanical scanning for B-scan imaging, which has led to 50 Hz real-time B-scan imaging; for 3D imaging, linear mechanical scanning is required, which, however, is still much faster than the raster scanning required by a system with a single-element ultrasonic transducer.

Currently, the high-speed photoacoustic imaging system performs real-time B-scan imaging at 50 Hz and 3D imaging of 166 B-scan frames at ~0.2 Hz, representing the highest speed in high frequency photoacoustic imaging to our knowledge. The temporal resolution, ~6 s, is currently limited by the data-saving and beamforming after each 3D image acquisition. It can be improved by temporarily storing all 3D data in computer memory during the entire data acquisition without beamforming, or by using a 48-channel DAQ card to eliminate the multiplexing—then one laser pulse instead of six could produce one B-scan image. We will explore both directions in the future.

In photoacoustic imaging, the spatial resolution and imaging depth are scalable with the ultrasonic frequency within the reach of photons [22]. With a 3.5 MHz single-element ultrasonic transducer and methylene blue dye (at a laser wavelength of 635 nm), photoacoustic imaging was demonstrated to be capable of imaging SLNs as deep as 31 mm in scattering biological tissue—greater than the mean SLN depth of 12 $\pm$ 5 mm in humans [80, 81]. However, a relatively long time (20 – 40 min) was required to acquire one 3D image with that system. In this study, we demonstrated accurate photoacoustic SLN mapping in mice and rats, as well as the capability to quantify the dye dynamics in SLNs. As the major goal of this study was to demonstrate the feasibility of capturing the dye dynamics in SLNs with photoacoustic imaging, the choice of the dye (Evans blue) and wavelength (600 nm), limited by the operating spectral range of our kHz repetition rate laser system, were not fully optimized for deep imaging. However, with the feasibility demonstrated in this study, we expect that a low-frequency ultrasound array (e.g., 3 –

5 MHz) and a high-power laser, operating at a longer wavelength (e.g., ~700 nm), will enable photoacoustic imaging to achieve a sufficient imaging depth (~30 mm), while retaining the high imaging speed. To translate the technology to the clinic, a high-speed photoacoustic imaging system with a commercial low-frequency ultrasound array is desired. Potentially, for noninvasive SLN mapping in clinics, such a system can offer advantages in precision, depth, and speed, and also provide co-registered complementary ultrasonic images.

5.5 Conclusions

SLNs in mice and rats were accurately mapped noninvasively *in vivo* using a high-speed 3D photoacoustic imaging system with a 30-MHz ultrasound array. The system achieved a speed for 3D photoacoustic imaging approaching 0.2 Hz, highly desirable in clinics. In addition, the dynamics of dye accumulation and clearance in the murine SLNs were quantitatively monitored with a high temporal resolution, up to 6 s. This capability should facilitate further studies to understand the dynamics of different dyes in SLNs, and potentially help identify SLNs with higher accuracy.

Chapter 6 Ultrasound-array-based Real-time Photoacoustic Microscopy of Human Pulsatile Dynamics *In vivo*[†]

6.1 Introduction

Due to the requirement for both high imaging speed and noninvasiveness, it remains challenging to precisely image and quantify human physiological dynamics *in vivo* in real time. MRI provides good functional imaging capability, but it usually cannot perform real-time imaging [94]. Ultrasound offers real-time imaging capability, but the mechanical contrast does not provide much physiological information besides flow [95]. Previously available high-resolution optical microscopy modalities—including confocal microscopy [96], two-photon microscopy [21], and optical coherence tomography [97]—are capable of real-time imaging. However, as none of them sense optical absorption directly, contrast agents are usually required for physiological imaging. Moreover, they rely on the detection of ballistic photons, and thus cannot image beyond one optical transport mean free path in highly scattering biological tissue (~1 mm).

Photoacoustic tomography is a recently developed, noninvasive biomedical imaging technology that provides excellent optical absorption contrast—endogenous contrast for many physiological phenomena—with high ultrasonic resolution at super-depths—depths beyond the optical transport mean free path [19]. It has been used to study whisker stimulation [34], single vessel oxygenation [1], and tumor hypoxia [24]. Photoacoustic tomography is also a high-speed imaging modality by nature, with its speed fundamentally limited by the photoacoustic wave propagation time. In principle, A-lines (i.e., depth-resolved 1D images) can be acquired at a rate of up to 100 kHz at a depth of 1.5 cm. With a 30-MHz ultrasound array and a kHz repetition laser

[†] Reused with permission from L. Song, K. Maslov, K. K. Shung, and L. V. Wang, "Ultrasound-array-based real-time photoacoustic microscopy of human pulsatile dynamics *in vivo*," *Journal of Biomedical Optics* **15**, 021303 (2010).

system, we have developed a photoacoustic microscopy imaging system that performs real-time B-scan imaging at 50 Hz and high-speed 3D imaging, offering the feasibility of imaging physiological dynamics [82-84]. In addition, this ultrasound-array-based photoacoustic microscopy (UA-PAM) system, with axial, lateral, and elevational resolutions of 25, 70, and 300 μm, respectively, provides ~3 mm imaging depth in scattering biological tissue [82].

In this study, with system refinement, we report significant improvement in the image quality of UA-PAM, which enabled the imaging of microvasculature details in rats and human. In addition, the 20 ms B-scan imaging temporal resolution offered the capability to noninvasively monitor human pulsatile dynamics—including arterial pulsatile motion and changes in hemoglobin concentration—*in vivo*. To our knowledge, this is the first demonstration of real-time photoacoustic imaging of human physiological dynamics.

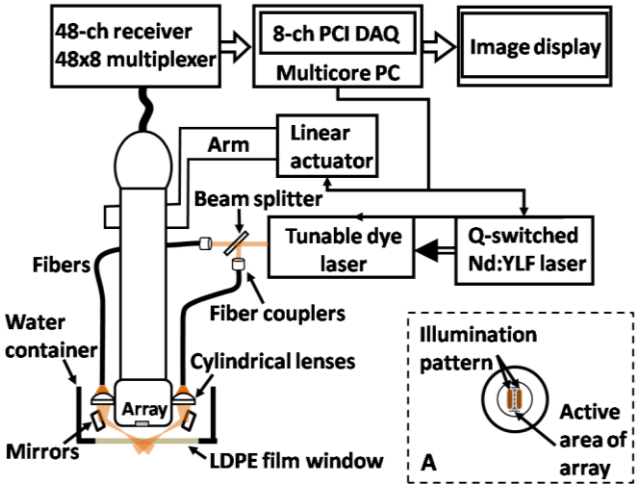

Figure 6.1. Schematic of the refined UA-PAM system. Inset A, optical illumination pattern on the skin surface.

6.2 Methods and materials

The system configuration is shown in Figure 6.1. The details of the system can be found in our previous publications [82-84]. In this work, to excite photoacoustic waves, we used light at 570 nm,

which corresponds to an isosbestic point where oxy- and deoxy-hemoglobin molecules have the same molar optical absorption coefficient.

To couple the generated photoacoustic waves to the ultrasound-array transducer, we used a water container (filled with de-ionized water) with a window of low-density polyethylene (LDPE) film, to substitute for the water-filled transparent plastic piece in our previous system [98, 99]. As a result, the skin surface was not directly contacted by the scanning probe during experiments, and disturbance to the imaged object was minimized. As before, acoustic gel was used to improve the ultrasonic coupling between the skin surface and the LDPE film. Compared with the previous system, the chances for air-bubble generation in the gel during the mechanical scanning (for 3D imaging) of the probe were significantly reduced, as both the skin and the film were static. Furthermore, the number of optical interfaces was reduced, which increased the light delivery efficiency. Fine-tuning of the light delivery was performed to optimize the system's signal-to-noise ratio [98, 99]. All animal and human experiments described below were carried out in compliance with Washington University approved protocols.

To validate the refined UA-PAM system, Sprague Dawley rats (Harlan Laboratories, Inc., USA) were imaged. Intra-dermal injection of a mixture of ketamine (85 mg/kg) and xylazine (15 mg/kg) was used for anesthesia. Before photoacoustic imaging, the hair in the imaged region was removed with commercial depilatory lotion.

The UA-PAM system is also safe for human use. For human imaging, the optical fluence on the skin surface was set to ~0.5 mJ/cm^2 per pulse, well below the ANSI [98, 99] recommended Maximum Permissible Exposure (MPE) of 20 mJ/cm^2 for a single pulse in the visible spectral range. For 10 s of continuous real-time B-scan imaging (at 50 Hz), 3000 laser pulses were delivered to the skin surface, corresponding to a time-averaged light intensity of ~150 mW/cm^2,

below the ANSI recommended MPE of 196 mW/cm^2, calculated by $1.1t^{0.25}$ W/cm^2. For 3D imaging, the laser pulse repetition rate was increased to 996 Hz. However, in this case, the total illuminated area was also increased due to the mechanical scanning of the probe, resulting in a time-averaged light intensity of ~300 mW/cm^2, below the 1.1 W/cm^2 ANSI safety standard based on the same calculation.

6.3 Results

An *in vivo* photoacoustic maximum amplitude projection (MAP) image—the maximum photoacoustic amplitudes projected along the depth direction to the skin surface—of a rat (Figure 6.2(A)) weighing ~280 g is shown in Figure 6.2(B). Compared with previous results [82], more microvasculature details were imaged with the refined UA-PAM system. Figure 6.2(C) is a B-scan image corresponding to the dashed line in Figure 6.2(B), showing subcutaneous blood vessels at various depths, up to 1 mm below the rat's skin surface. The imaged blood vessels are of diameters ~70 – 300 μm. To view the vasculature from different perspectives, a 3D animation (Video 1), showing blood vessels in different layers, was constructed with VolView (Kitware, USA). More features, including rotation, scaling, and zooming, are available with the software.

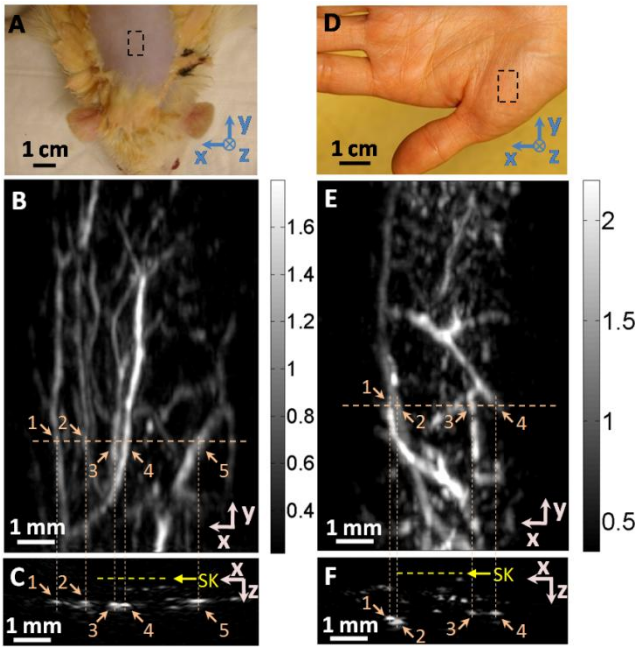

Figure 6.2. Noninvasive *in vivo* photoacoustic images acquired by the refined UA-PAM system. (A) Photograph of a Sprague Dawley rat with hair removed before photoacoustic imaging. *x* represents the beamforming (B-scan) direction, *y* represents the mechanical scanning direction, and *z* represents the depth direction. The dashed rectangle indicates the imaged area. (B) Photoacoustic maximum amplitude projection (MAP) image of the rat. The grayscale represents relative optical absorption. (C) Photoacoustic B-scan image corresponding to the dashed horizontal line in (B), showing the depths of the blood vessels. SK, skin surface. Numbers 1 – 5 indicate corresponding blood vessels in (B) and (C). (D) Photograph of a human hand. The dashed rectangle indicates the imaged area. (E) Photoacoustic MAP image of the hand. (F) Photoacoustic B-scan image corresponding to the dashed horizontal line in (E). Numbers 1 – 4 indicate corresponding blood vessels in (E) and (F).

To demonstrate the feasibility of human imaging with UA-PAM, we imaged the palm of a human hand (Figure 6.2(D)). The subcutaneous microvasculature of the hand was imaged, with

a quality comparable to that of the aforementioned rat images. The imaged blood vessels in the human hand are bigger though, ranging from ~100 to 400 μm (Figure 6.2(E)). The depths of the blood vessels were clearly shown in the B-scan image (Figure 6.2(F)). Subcutaneous blood vessels up to 1.2 mm deep were imaged in this case. Due to the overlap, some relatively small blood vessels are not well shown in the MAP image. However, these vessels, along with the layered vascular structures, are clearly seen in the 3D animation (Video 2).

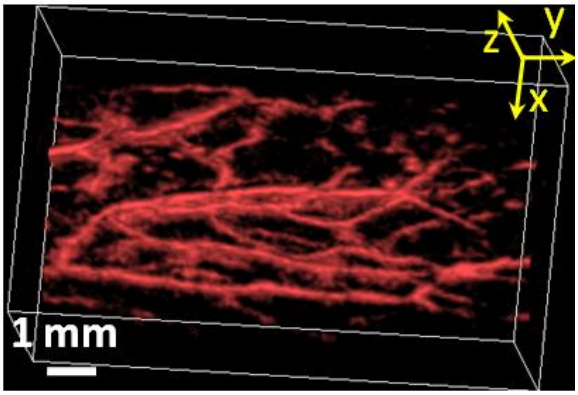

Video 1. Photoacoustic 3D animation of the rat (MOV, 4.05 MB).

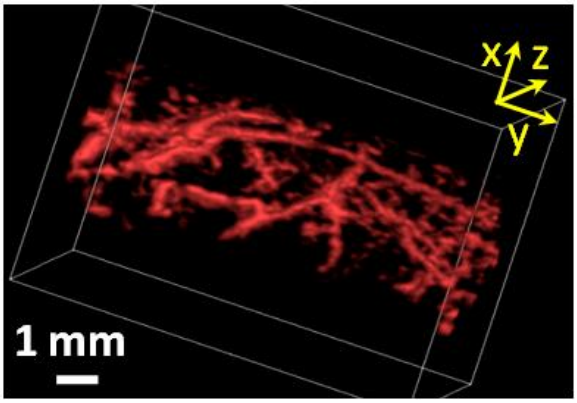

Video 2. Photoacoustic 3D animation of the human hand (MOV, 4.50 MB).

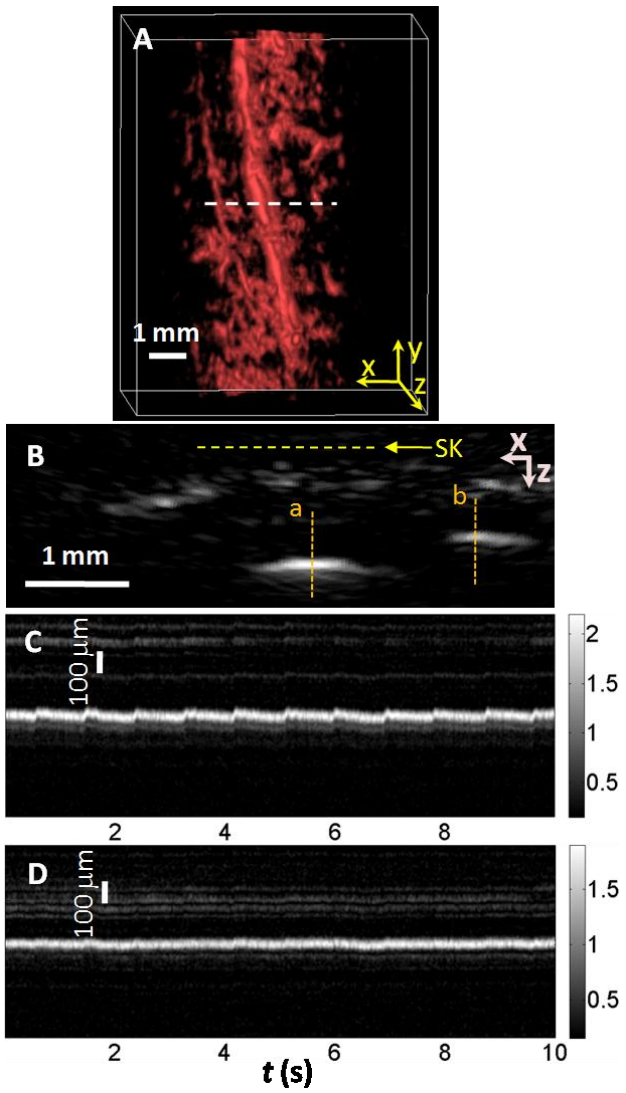

Figure 6.3. Dynamic noninvasive *in vivo* photoacoustic imaging by the refined UA-PAM system. (A) *In vivo* 3D photoacoustic image of a human hand. The dashed line indicates the cross-section monitored by real-time B-scan imaging. (B) One B-scan image corresponding to the dashed horizontal line in (A). SK, skin surface. (C) M-mode image corresponding to the dotted vertical line *a* in (B), showing the arterial pulsatile motion as a function of time. (D) M-mode image of a vein corresponding to the dotted vertical line *b* in (B).

To study the pulsatile dynamics, we scanned a region of the palm near the wrist, where an apparent artery, ~1 mm in diameter and over 1 mm deep, was imaged (Figure 6.3(A)). After acquiring the initial 3D image, we fixed the scanning probe to perform 10-s real-time B-scan imaging across the artery (Figure 6.3(B) and Video 3). Due to the strong optical absorption of hemoglobin at 570 nm (absorption coefficient $\mu_a \approx 200$ cm^{-1}), the bottom part of the artery was not well-imaged. But the motion dynamics of the arterial pulsation was clearly captured. An M-mode image across the center of the artery, showing the details of the pulsatile motion, is shown in Figure 6.3(C). The pulsatile rate, estimated from the image, was 66 per minute, consistent with the 65 ± 2 per-minute rate measured from a pulse oximeter. For comparison, an M-Mode image of a vein was plotted in Figure 6.3(D), from which weak motion of the vein was revealed. Presumably, the motion was due to artery-pulsation-induced skin movement (observable in Video 3). As seen from Figure 6.3(D), the vein's motion was indeed weakly correlated with the artery pulsation. However, compared with the artery (Figure 6.3(C)), the vein's motion was much weaker.

To supplement tissue structural information, and to validate the observed artery motion, we acquired ultrasound images of similar regions using a commercial ultrasound machine (iU22 with a L15-7io Compact Linear Array, Philips). The ultrasound transducer, covering frequencies ~7 – 15 MHz, provides sufficient resolution to resolve the artery that was photoacoustically imaged. In the ultrasound images, it was interesting to see that the artery only expanded apparently in the direction normal to the skin surface (Video 4). In the direction parallel to the skin surface, the expansion was almost negligible. This type of motion was likely due to the anisotropy of the surrounding tissue structure, namely, the surrounding tissue can be more easily stretched perpendicularly to the skin surface than parallelly to the skin surface. The

observed motion in the ultrasound images was consistent with the result seen in real-time photoacoustic imaging, where apparent motion was observed only in the skin's normal direction. In addition, the M-mode images acquired with our UA-PAM system agreed well with those acquired by the commercial ultrasound machine, which, however, didn't show as much fine details as the UA-PAM system did.

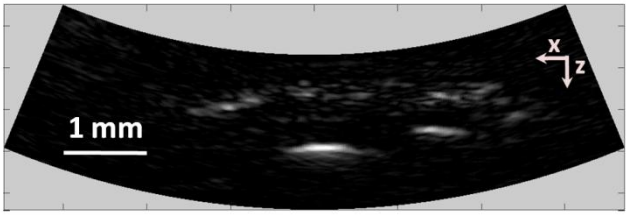

Video 3. Real-time photoacoustic B-scan imaging of the arterial pulsation (MOV, 690 KB).

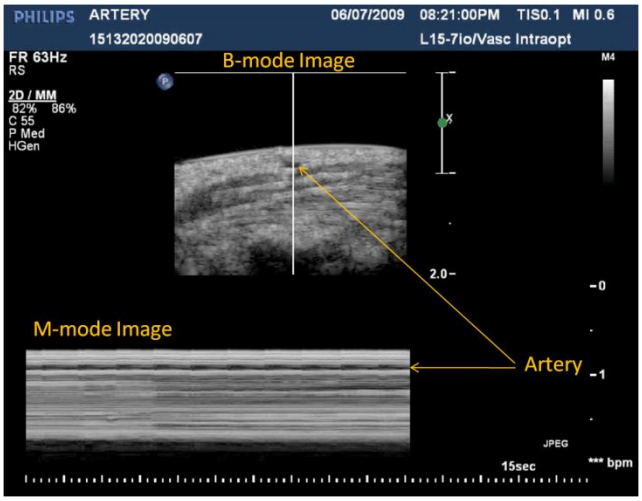

Video 4. Ultrasound images of the arterial pulsation. The up-panel shows B-mode images, while the bottom one shows M-mode images corresponding to the vertical line in the up-panel (MOV, 2.84 MB).

6.4 Discussion and conclusions

One drawback of ultrasound imaging is that little physiological information besides flow can be provided. By contrast, photoacoustic imaging has the potential to offer both hemoglobin concentration and oxygen saturation information. Ideally, to better characterize the pulsatile hemodynamics, oxygen saturation should be measured within each cardiac cycle. However, accurate computation of the blood oxygenation in real-time requires photoacoustic imaging with laser-wavelength tunability in real time (because oxygenation quantification requires multi-wavelength measurements), which is currently not available in our laser system. Fortunately, the change in hemoglobin concentration can be monitored already with UA-PAM. Although the arterial pulsatile motions were apparent (Figure 6.3(C) and Video 3), we found that the hemoglobin concentration was approximately constant with time—the standard deviation of the signal normalized by the temporal maximum value was 0.02. We also studied the hemoglobin concentration dynamics of a vein, which showed similar results. This observation agreed with the fact that, under normal physiological conditions, the hemoglobin concentration does not change significantly.

A few factors—including hemoglobin concentration, oxygenation, and vessel diameter and position—can potentially affect the magnitude (instead of position) of the received photoacoustic signal; in general, they may not be decoupled easily. In this study, however, we believe that any observable change in the magnitude of the signal, if any, would be due primarily to the hemoglobin concentration variation. Conversely, the lack of such change in the observable signal suggests that the hemoglobin concentration was approximately constant. Our reasoning is as follows:

- The 570 nm wavelength that we used corresponds to an isosbestic point; therefore, oxygenation does not affect the photoacoustic signal.
- In principle, without considering the limited acoustic receiving aperture and reconstruction imperfection, the signal should be proportional to the square root of the vessel diameter [19]. With a blood-vessel-mimicking phantom of ~1 mm diameter, we found that, a 15% diameter variation would induce only ~2% signal change, smaller than the theoretical value. Given the ~2% noise level (without averaging), only greater diameter variations can generate observable signal changes. In addition, the vaso-dilation was apparent only in the depth direction, further reducing the dilation-induced signal change, and making it essentially negligible.
- Experiments with phantoms also showed that, around the acoustic elevational focus, a 50 μm displacement in the depth direction would induce only a ~1.5% signal change. In fact, during our experiment, we did not observe any significant change of the artery position. Even if we took into account the vaso-dilation induced displacement (~50 μm), the signal change would still be negligible.

In summary, our refined UA-PAM system performed high-speed *in vivo* imaging of microvasculature details in both rats and humans with improved quality. With this UA-PAM system, hemoglobin concentration dynamics and arterial pulsatile motion were captured in real time, for the first time, to our knowledge. With the promising results shown in this study, we believe that UA-PAM will open up many new possibilities for studying functional and physiological dynamics in both preclinical and clinical imaging settings.

Chapter 7 Section-illumination Photoacoustic Microscopy for Dynamic 3D Imaging of Microcirculation *In vivo*[†]

7.1 Introduction

The microcirculation of blood plays a crucial role in the regulation of hemodynamics and metabolism; its physiological state can indicate many diseases, including diabetes, hypertension, and coronary heart disease. Hence, the study of microcirculation is vital to both clinical practice—e.g., the evaluation of tissue perfusion in the presence of vascular diseases—and preclinical studies—e.g., the assessment of therapeutic efficacy in drug development [100-102]. Many complementary imaging techniques—including nailfold capillaroscopy, polarization spectral imaging, high-frequency ultrasound imaging, and magnetic resonance imaging—have been used to study microcirculation [102-105]. Yet none of them simultaneously offer desired sensitivity, resolution, and imaging depth in a single modality.

Recently, optical-resolution photoacoustic microscopy (OR-PAM) has emerged as a viable tool for *in vivo* microvascular imaging [106]. OR-PAM provides high optical absorption contrast—from either intrinsic or exogenous absorbers—and axial ultrasonic resolution at depths up to the optical transport mean free path (~1 mm in the skin) [2]. If a single-element ultrasonic transducer is used, the imaging speed is limited by the 2-D mechanical scanning for 3D imaging. One solution to improving the speed is to use an ultrasound array. Previously, an ultrasound array was used to accelerate the imaging rate of acoustic-resolution photoacoustic microscopy (AR-PAM) by ~100-fold from the single-element implementation—reaching a B-scan imaging rate of 166 Hz, a 3D imaging rate of ~0.1 Hz, and a single 3D imaging time of only 1–2 s [54, 99]. However,

[†] Reused with permission from L. Song, K. Maslov, and L. V. Wang, "Section-illumination photoacoustic microscopy for dynamic 3-D imaging of microcirculation *in vivo*," *Optics Letters* **35**, 1482 (2010).

the poor acoustic elevational focus (>200 μm)—common to all linear ultrasound arrays—became a bottleneck for spatial resolution [98, 107], which limited its application in microcirculation studies (most microvessels have diameters less than 100 μm).

In this work, we developed section-illumination photoacoustic microscopy (SI-PAM) to improve the elevational resolution. Moreover, by optimizing data acquisition and transfer, we improved the imaging speed to 249 Hz for B-scans and 0.5 Hz for continuous 3D scans. SI-PAM was used to image *in vivo* microcirculation dynamics in mouse ears noninvasively. To our knowledge, this is the first report of dynamic 3D *in vivo* photoacoustic imaging with both high temporal and spatial resolutions.

7.2 Methods

The principles of SI-PAM are shown in Figure 7.1. In order to achieve section illumination, the laser beam was first expanded, and then cylindrically focused into the sample. The numerical aperture of the focus was 0.015, which in theory would result in an elevational resolution of 24 μm—10-fold better than the one defined acoustically; the depth of focus in air was ~2.7 mm, greater than the targeted 1-mm imaging depth. To detect the photoacoustic waves from the sample, a custom-built ultrasound array of 30-MHz center frequency was used, positioned opposite the laser illumination. Photoacoustically exciting the entire B-scan imaging region with each laser pulse, the section illumination was able to take full advantage of the ultrasound array for high-speed imaging. While 2-D B-scan imaging required no mechanical scanning, 3D imaging necessitated linearly translating the sample in the elevational (*y*) direction. By storing photoacoustic signals in the data acquisition (DAQ) card, we achieved 3D image acquisition at 0.5 Hz, corresponding to a 2-D (B-scan) image acquisition rate of 249 Hz. Currently, in order to stream data from the 48-channel ultrasound array to the 8-channel DAQ card, 6 laser pulses

were needed for one B-scan. Thus the laser repetition rate corresponding to the 249-Hz B-scan rate was ~1.5 kHz, approximately the highest rate at which our laser could operate. Further details about image acquisition and reconstruction were presented in our previous publications [54, 99].

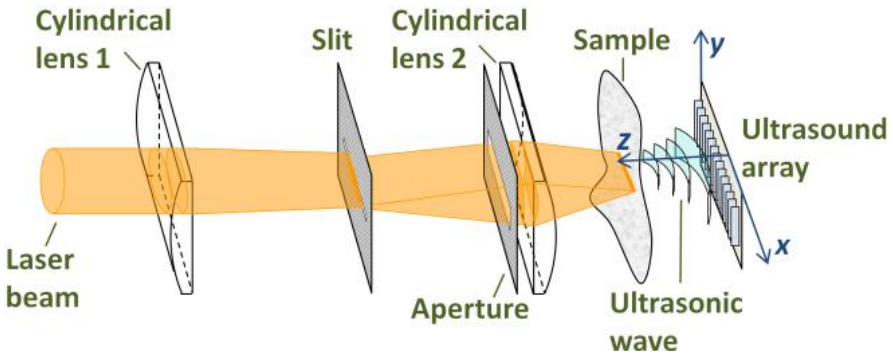

Figure 7.1. (Color online) Schematic of the section-illumination photoacoustic microscopy (SI-PAM) system. The widths of the slit and the aperture along the *y* axis are 50 μm and 5 mm, respectively. Coordinates *x*, *y*, and *z* represent the lateral, elevational, and axial (depth) directions of the ultrasound array, respectively.

7.3 Results

Figures 7.2(a)–(c) show that the elevational resolution (*y*) was improved ~10 fold—from 200–400 μm to 28 μm—by the section illumination, while the in-plane lateral (*x*) resolution (~70 μm) was unaffected. Figure 7.2(d) shows that SI-PAM can penetrate ~1.6 mm through biological tissue. Figure 7.2(e) is an *in vivo* photoacoustic image of a mouse ear microvasculature acquired by SI-PAM at 584 nm, sensing the intrinsic absorption contrast of hemoglobin. The image is shown in the form of maximum amplitude projection (MAP)—the maximum photoacoustic amplitudes projected along a direction to its orthogonal plane—along the *z* axis with depth encoded by color. Unless otherwise mentioned, all MAPs are along the *z* axis. Microvessels in diameters down to 30 microns were clearly imaged, and a predominantly two-layered structure

of blood vessels was observed, consistent with the previous results from OR-PAM [108]. Figure 7.2(f) is a snapshot of a 3D animation (Video 1) showing the mouse ear microvasculature from various perspectives. All animal experiments were carried out complying with Washington University approved protocols.

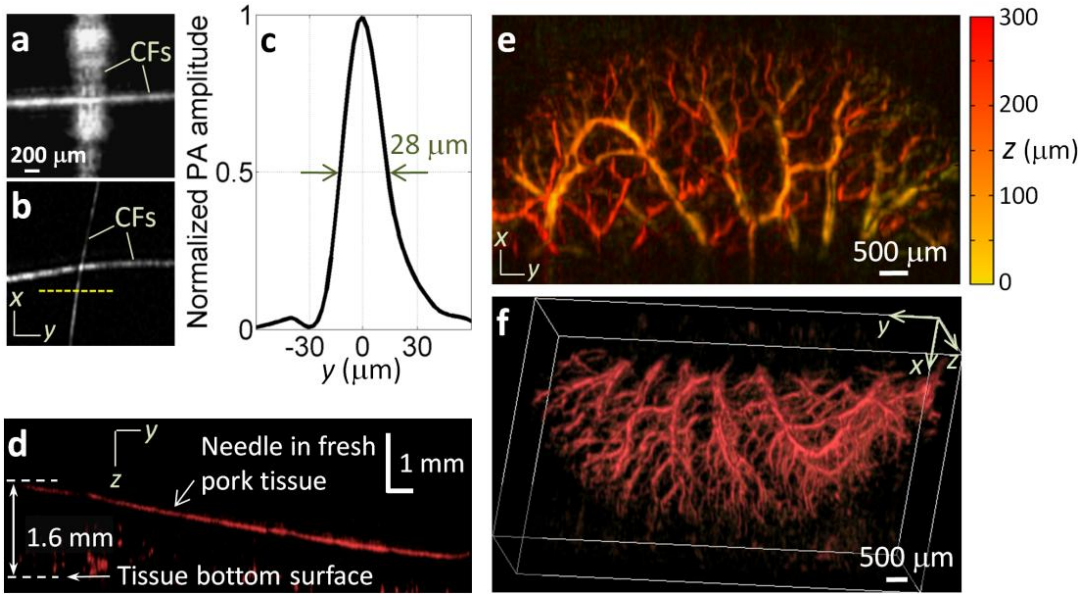

Figure 7.2. (Color online) (a,b) MAP images of two crossed 6-μm diameter carbon fibers (CFs) acquired by PAM at 584 nm without and with section illumination, respectively. (c) Distribution of photoacoustic (PA) amplitude from the vertical carbon fiber along the dashed line in (b). (d) MAP (along the *x* axis) image of a 250-μm diameter black needle inserted in a fresh pork specimen acquired by SI-PAM at 584 nm. (e) MAP image of a mouse ear microvasculature acquired by SI-PAM noninvasively *in vivo* (at 584 nm). Depth (*z*)—300 μm in total—is encoded by color. (f) Snapshot of a 3D animation (Video 1) showing the microvasculature in (e).

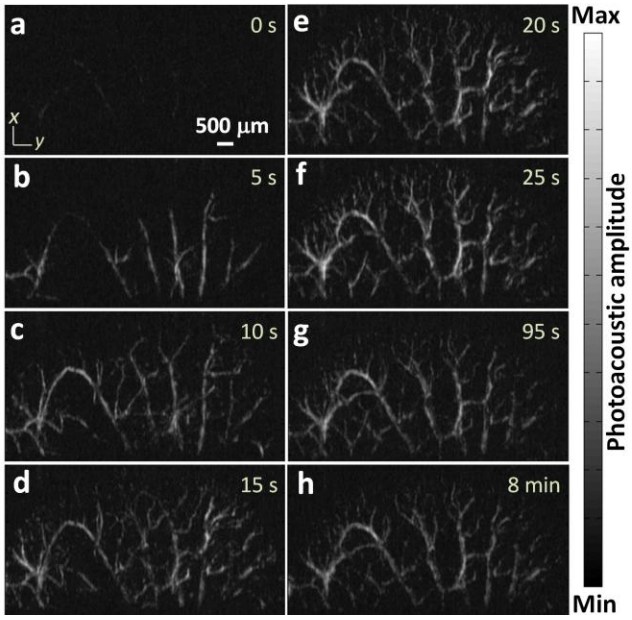

Figure 7.3. (Color online) Wash-in dynamics of EB in a mouse ear microvasculature imaged by SI-PAM at 600 nm (Video 2). (a)–(h) MAP images at representative time points after EB injection.

The dynamic 3D *in vivo* imaging capability of SI-PAM was demonstrated by real-time monitoring of the wash-in dynamics of Evans Blue (EB) dye in mouse ear microcirculation. Swiss Webster mice (Harlan, Inc., USA) weighing ~25 g were used. Upon injection of ~0.05 ml of 3% EB through the tail vein, the mouse ear was continuously imaged by SI-PAM at 600 nm for up to 2 min at 5-s intervals. At this wavelength, EB has much stronger absorption (which peaks at 620 nm) than hemoglobin, and thus its signal dominates the contrast. Video 2 shows the entire EB wash-in process recorded by SI-PAM—with representative frames shown in Figure 7.3. It is clearly seen that the dye progressively reaches different levels of vessel branches—from the root to the edge of the ear—at different time points. Yet the overall wash-in process is as short as 15–20 s. After 1–2 min, the photoacoustic signal decreases (Figures 7.3(g) and (h)), indicating

the beginning of the wash-out of EB. However, the entire wash-out process, which was not monitored in this study, could take up to a few days.

Although the spatial resolution of the SI-PAM was insufficient to resolve closely located arteriole-venule pairs even if the oxygen saturation of hemoglobin were measured spectrally, we found that the dynamics enabled us to distinguish arterioles from venules in the microcirculation. In fact, four distinct stages of the wash-in process can be observed in Video 2 (or Figure 7.3):

1. EB dye flowed to the major arterioles at the root of the ear;
2. EB dye reached the arteriole branches and the capillary bed at the edge of the ear;
3. EB dye returned to the venule branches from the capillary bed;
4. EB dye returned to the major venules at the root of the ear.

In the end, the entire microcirculation of the mouse ear was perfused with EB dye. Figure 7.4 is a pseudo-colored composite image showing the separated arterioles (red) and venules (green). Furthermore, Video 3 shows the wash-in dynamics of EB in both grayscale and pseudo-color.

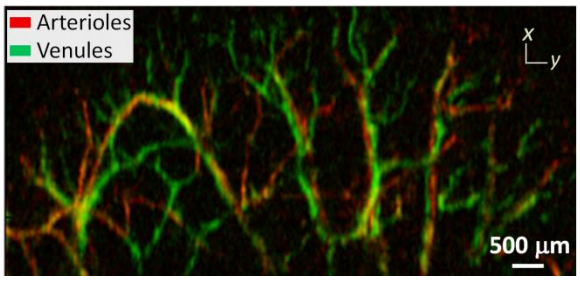

Figure 7.4. (Color online) Pseudo-colored composite image showing arterioles and venules separated according to the wash-in dynamics of EB (Video 3).

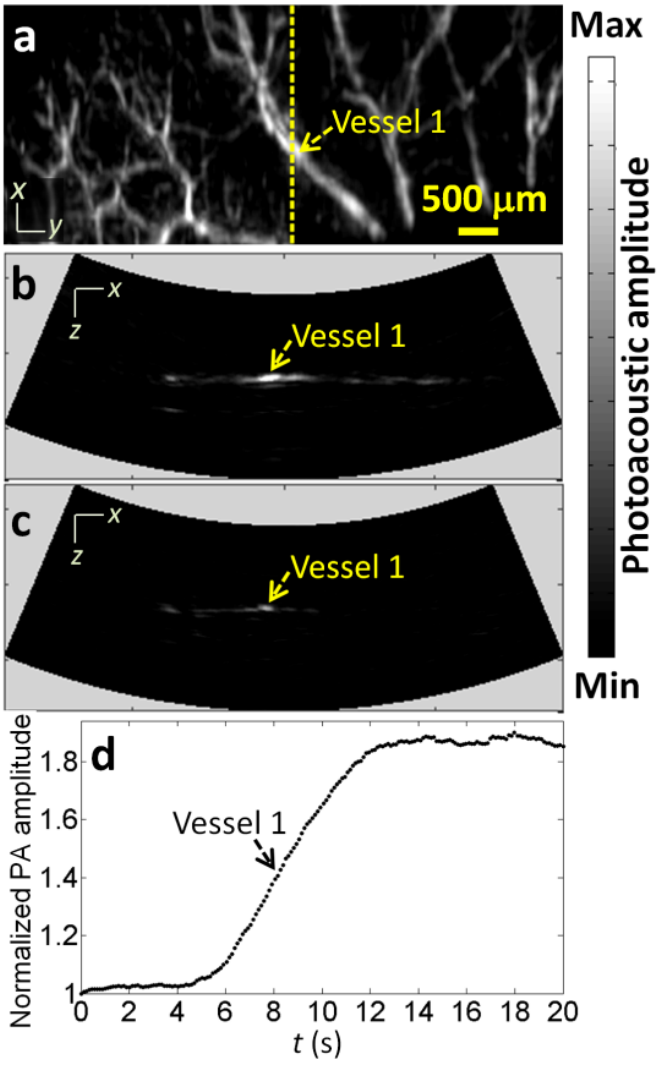

Figure 7.5. (Color online) Real-time B-scan imaging of the EB wash-in dynamics in a mouse ear microvasculature. (a) Control MAP image at 584 nm. (b) Control B-scan image at 584 nm corresponding to the dotted line in (a). (c) Snapshot of a B-scan movie of the EB wash-in dynamics acquired at 600 nm (Video 4). (d) Plot of the EB wash-in dynamics in vessel 1.

With 50 Hz B-scan imaging rate, the entire EB uptake process was quantitatively imaged by SI-PAM. An MAP image and a representative B-scan image of the mouse ear microvasculature are shown in Figures 7.5(a) and (b), respectively. Video 4 is a real-time B-scan movie showing

the EB uptake in a single vessel (vessel 1). The photoacoustic amplitude representing the dye concentration was quantified as a function of time (Figure 7.5 (d)). The EB injection started at *t* = 0 s and took ~2 s to complete. At ~14 s, the photoacoustic signal stabilized, suggesting that the dye concentration had reached a steady state in the blood circulation. This stabilization time agreed well with the circulation time needed to fully mix the dye in blood, which was ~15 s as estimated by using a stroke volume of 20 μl, a heart-beat rate of 400 beats/min (mice under anesthesia), and a total blood volume of 2 ml.

7.4 Conclusions

In summary, we developed section-illumination photoacoustic microscopy (SI-PAM) that overcomes the poor elevational resolution bottleneck of ultrasound array photoacoustic microscopy: the system offers 28-μm elevational, 25-μm axial, and 70-μm lateral resolutions. In addition, SI-PAM is capable of B-scan and 3D image acquisition at 249 and 0.5 Hz, respectively. The combined high spatial and temporal resolutions enable dynamic 3D imaging of microcirculation *in vivo*. Using SI-PAM, the wash-in dynamics of EB in mouse ear microcirculation were noninvasively imaged and quantified. Major arterioles and venules were differentiated using the EB wash-in dynamics. In the future, to enable the imaging of more anatomical sites *in vivo*, reflection-mode SI-PAM will be constructed. With this successful demonstration of dynamic 3D *in vivo* imaging of microcirculation, we believe that SI-PAM will open up many new possibilities for the study of angiogenesis, diabetes-induced vascular complications, and pharmacokinetics.

Chapter 8 Multi-focal Optical-resolution Photoacoustic Microscopy

8.1 Introduction

Due to the vital role of the microcirculation in the regulation of hemodynamics and metabolism, imaging of the microvasculature is crucial to both clinical practice and preclinical research [101]. Many high-resolution optical imaging modalities—including confocal microscopy, two-photon microscopy, and optical coherence tomography—have been adopted for microvascular imaging [109-112]. However, they either require exogenous fluorescent agents or have insufficient sensitivity to image a single capillary. In addition, none of them have direct access to the total concentration and oxygen saturation (sO_2) of hemoglobin—two important functional parameters in disease diagnosis [113].

In contrast, optical-resolution photoacoustic microscopy (OR-PAM) provides extremely high sensitivity to optical absorption (for example, the intrinsic optical absorption of oxy- and deoxy-hemoglobin), with optical diffraction limited lateral resolution [106]. It is capable of imaging both the total concentration and sO_2 of hemoglobin in microvessels—including capillaries—*in vivo*, making it a viable tool for microvascular imaging [108, 114]. However, the imaging speed of OR-PAM with single-element ultrasonic detection is usually limited by its mechanical scanning. Previously, to improve the imaging speed of OR-PAM, a Galvo mirror was used to rapidly scan the illumination laser beam confined within the field of view of an unfocused ultrasonic transducer [115]. A hybrid optical-mechanical scanning OR-PAM was also developed, using a Galvo mirror and a cylindrically focused ultrasonic transducer [116]. However, since the ultrasonic transducer was either unfocused or focused in only one axis, the signal-to-noise (SNR) ratio of the system was inherently limited. In addition, because only a single laser beam and a single ultrasonic transducer were used, these systems demand a laser pulse repetition rate as high as 5

– 10 kHz to significantly improve the imaging speed. Presently, lasers with such high pulse repetition rates (and sufficient pulse energy for OR-PAM) usually lack the wavelength tunability needed for measuring the sO_2 of hemoglobin.

In this work, we developed an alternative method—using multi-focal optical illumination in conjunction with ultrasonic array detection—to improve the imaging speed of OR-PAM. For photoacoustic excitation, a microlens array was used, providing 20 focused optical illumination spots; for ultrasonic detection, a linear ultrasound array was used, detecting photoacoustic emissions from all illumination beams simultaneously. The signals from different sites were separated using photoacoustic reconstruction algorithms [99, 107, 117]. With a tunable dye laser operating at a ~1.3-kHz pulse repetition rate, our multi-focal optical-resolution photoacoustic microscopy (MFOR-PAM) system was capable of imaging both the concentration and sO_2 of hemoglobin in microvessels *in vivo*, at an imaging speed significantly faster than that of a mechanical scanning single-focal OR-PAM system. Of note, the use of the ultrasound array with photoacoustic reconstruction allows the spacing between adjacent optical illumination beams to be as small as the lateral resolution of the ultrasound array. Fundamentally different from simply combining multiple assemblies of a single optical focusing element and a single ultrasonic transducer, this approach enables us to position optical foci much closer to each other and potentially to scan optically at high speed.

8.2 Methods

Figure 8.1 illustrates the basic principles of MFOR-PAM. To provide multi-focal optical illumination for photoacoustic excitation, the laser beam from a pulsed laser system (a tunable dye laser pumped by an Nd:YLF laser) was first expanded, and then cylindrically focused onto a microlens array. The full width at half maximum (FWHM) of the cylindrically focused incident

laser beam approximately matched the 250-μm width (along *y*) of the microlens array, resulting in 20 focused optical illumination spots along *x*. The distance between two nearby spots, determined by the pitch of the microlens array, was 250 μm, greater than the ~80-μm acoustic lateral resolution of our ultrasound array. The ultrasound array, with a center frequency of 30 MHz, has a 2-mm elevational aperture (along *y*) and consists of 48 elements along *x*, with a spacing of 100 μm. To acquire a volumetric image, the sample was scanned first along *y*, and then *x*, in the *x*-*y* plane. Due to the simultaneous photoacoustic excitation from the 20 illumination beams, the number of scanning steps along *x* was reduced 20-fold compared with that in conventional single-focus OR-PAM. In theory, this reduction could result in a 20-fold increase in imaging speed.

In our system, as a proof of concept, data from the 48-channel ultrasound array are multiplexed to an 8-channel data acquisition card, reducing the possible speed increase by 6 times. However, even with the multiplexing, our MFOR-PAM system can acquire a data set of 1000 × 500 × 200 voxels within 4 min, three to four times faster than existing mechanical scanning single-focus OR-PAM.

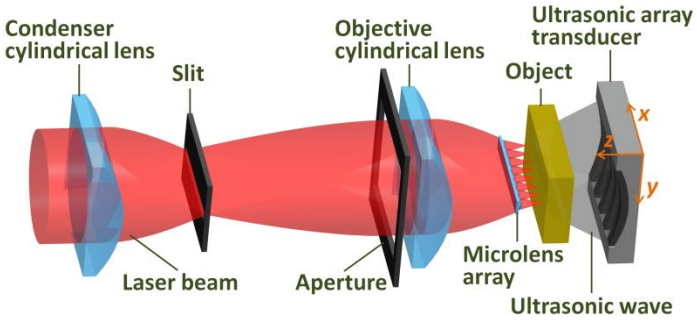

Figure 8.1. (Color online) Schematic of the multi-focal optical-resolution photoacoustic microscopy system. The widths of the slit and the aperture along *y* are 50 μm and 5 mm, respectively.

8.3 Results

As measured previously, the axial resolution of our system, determined by the receiving ultrasonic bandwidth, is ~25 μm [99]. To quantify the lateral resolution, which is determined by the optical focus of the microlens array, we imaged two 6-μm diameter crossed carbon fibers, using a scanning step of 2.5 μm. Figure 8.2(a) shows a maximum amplitude projection (MAP) image of the two carbon fibers. In this report, all MAP images were formed by projecting the maximum photoacoustic amplitudes along the *z* axis to the *x*-*y* plane. Figure 8.2(b) shows the FWHM of the vertical fiber, demonstrating that the lateral resolution of our system is at least as fine as 10 μm. The contrast-to-noise ratio (CNR), measured from Figure 8.2(a), is as high as 38 dB.

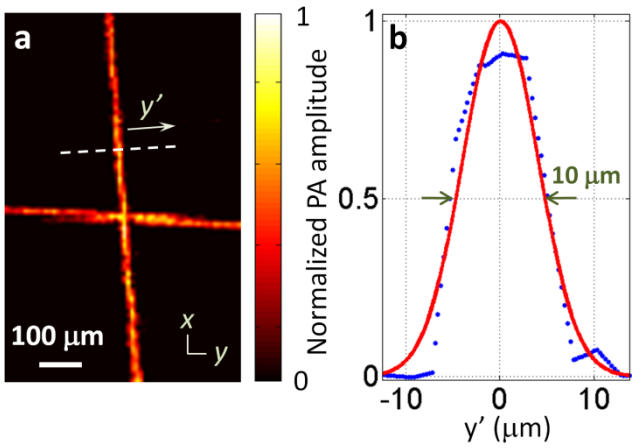

Figure 8.2. (Color online) Lateral resolution of the multi-focal optical-resolution photoacoustic microscopy system. (a) Photoacoustic (PA) maximum amplitude projection (MAP) image of two crossed 6-μm diameter carbon fibers. (b) Distribution of the PA amplitude (dots) along the dashed line in (a); the solid line is a Gaussian fitted curve.

To demonstrate the *in vivo* imaging capability of our system, we imaged the microvasculature in the right ear of a nude mouse (Hsd, Athymic Nude-Foxn1NU, Harlan Co.) weighing ~20 g. In order to couple the photoacoustic waves to the ultrasound array, a thin layer of ultrasonic gel was applied to the mouse ear. The image was acquired completely noninvasively, without using any optical clearing agent. After imaging, the animal naturally recovered without observable laser damage. All experimental animal procedures were carried out in compliance with protocols approved by the Animal Studies Committee of Washington University.

Figure 8.3(a) shows an *in vivo* MAP image of the mouse ear microvasculature acquired by our MFOR-PAM system at 570 nm, sensing the intrinsic optical absorption contrast of hemoglobin. Microvessels in diameters down to 10 μm are clearly imaged. Figure 8.3(b) is a snapshot of a 3D animation (Video 1) showing the mouse ear microvasculature from various perspectives. In addition to 570 nm, laser light at 565 nm was also used to image the mouse ear, enabling sO_2 measurement, as demonstrated previously with OR-PAM [108, 114]. While Figure 8.3(c) shows the microvasculature of a selected area, Figure 8.3(d) shows the corresponding vessel-by-vessel sO_2 mapping, where the arteries and veins are differentiated based on the measured sO_2. On average, the sO_2 values in arteries and veins were estimated to be 0.96 ± 0.4 and 0.75 ± 0.5, respectively, consistent with previous results from OR-PAM. In the experiment, the incident laser pulse energy on each microlens was limited to ~100 nJ, resulting in a maximum fluence of ~8 mJ/cm^2 on the skin surface (assuming the optical focus was 200 μm below the skin), which is less than the 20-mJ/cm^2 ANSI laser safety standard [61].

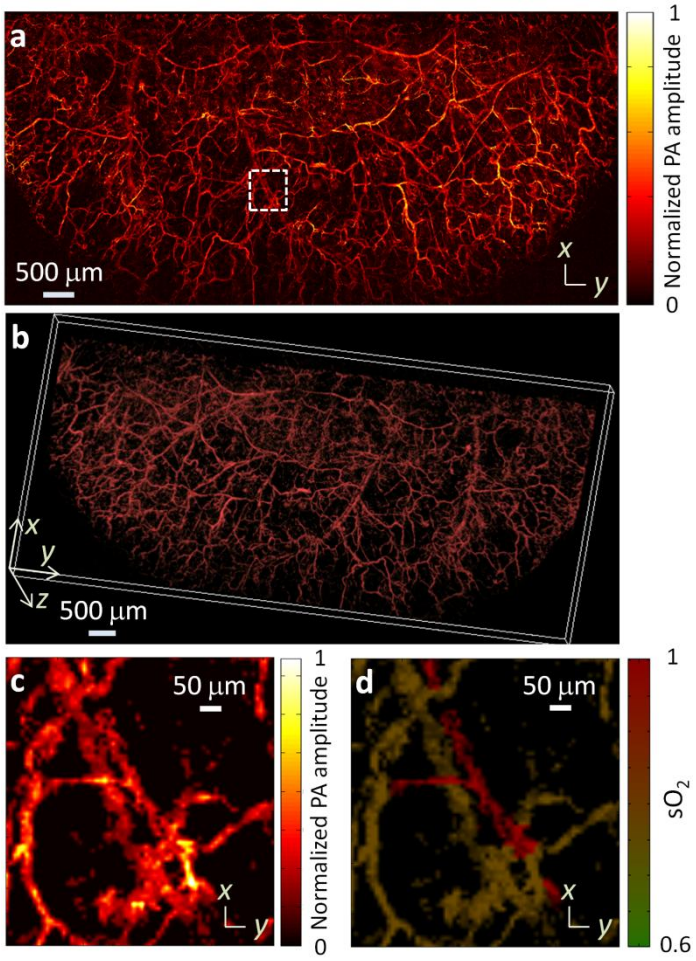

Figure 8.3. (Color online) *In vivo* photoacoustic image of a mouse ear microvasculature. (a) MAP image acquired at 570 nm. (b) Snapshot of a 3D animation (Video 1) showing the microvasculature in (a). (c) Close-up of the vasculature in the dashed box in (a). (d) Oxygen saturation (sO_2) mapping for vessels in (c).

8.4 Discussion and conclusions

In summary, using a microlens array and a high-frequency linear ultrasound array, we developed multi-focal optical-resolution photoacoustic microscopy. The system provided volumetric imaging of optical absorption contrast in scattering biological tissue *in vivo*, at depths up to the optical transport mean free path (~1 mm in the skin), and with optical diffraction limited lateral

resolution at least as fine as 10 μm. The axial resolution, determined by the receiving ultrasonic bandwidth, was ~25 μm. With this high spatial resolution and multiple wavelengths, our system was capable of imaging both the concentration and oxygen saturation of hemoglobin in capillary-level microvessels *in vivo*. Moreover, in MFOR-PAM, the combination of multi-focal optical illumination and ultrasonic array detection enabled a significant improvement in imaging speed over existing mechanical scanning single-focal OR-PAM. In the future, by eliminating the 6:1 multiplexing in data acquisition, the imaging speed can be increased 6-fold. In addition, a more densely packed microlens array (e.g., with a spacing of 100 μm), together with optical scanning within the lens array pitch, can be used to further increase the imaging speed. In clinical practice, high imaging speed is critical to reduce motion artifacts, cost, and patient discomfort. This proof-of-principle study has demonstrated that MFOR-PAM represents a promising direction for translating photoacoustic microscopy technology to the clinic.

Chapter 9 Summary

This dissertation presents our development of a novel high-speed, high-resolution photoacoustic microscopy technology and the experimental demonstrations of its potential biomedical applications. To translate PAM to the clinic, both high imaging speed and high spatial resolution are desired. With high spatial resolution, PAM can detect small structural or functional changes early; whereas, high-speed image acquisition helps reduce motion artifacts, patient discomfort, cost, and potentially the risks associated with minimally invasive procedures such as endoscopy and intravascular imaging.

In **Chapter 1**, we briefly introduce photoacoustic imaging technology, its unique advantages over existing imaging technologies, and its potential biomedical applications.

In **Chapter 2**, we present a novel high-frequency photoacoustic microscopy system capable of imaging the microvasculature of living subjects in real time to depths of a few millimeters. The system consists of a high-repetition-rate Q-switched pump laser, a tunable dye laser, a 30-MHz linear ultrasound array transducer, a multichannel high-frequency data acquisition system, and a shared-RAM multi-core-processor computer. Data acquisition, beamforming, scan conversion, and display are implemented in real-time at 50 frames per second. Clearly resolvable images of 6-μm-diameter carbon fibers are experimentally demonstrated at 80-μm separation distances. Real-time imaging performance is demonstrated on phantoms and *in vivo* with absorbing structures identified to depths of 2.5 – 3 mm. To our knowledge, this work represents the first high-frequency real-time photoacoustic imaging system.

Non-invasive visualization of cardiovascular dynamics in small animals is challenging due to their rapid heart rates. **In Chapter 3**, we demonstrate the ability of our real-time PAM system to

image optically-absorbing structures of the beating hearts of young athymic nude mice at rates of ~50 frames per second with 100 μm × 25 μm spatial resolution. To our knowledge, this is the first report of real-time photoacoustic imaging of physiological dynamics.

In Chapter 4, we present an *in vivo* dark-field reflection-mode photoacoustic microscopy system that performs cross-sectional (B-scan) imaging at 50 Hz with real-time beamforming and 3D imaging, consisting of 166 B-scan frames at 1 Hz, with post-beamforming. A custom-designed light delivery system is integrated with a 30-MHz ultrasound linear array to realize dark-field reflection-mode imaging. Linear mechanical scanning of the array produces 3D images. The system has axial, lateral, and elevational resolutions of 25, 70, and 200 μm, respectively, and can image 3-mm deep in scattering biological tissue. Volumetric images of subcutaneous vasculature in rats are demonstrated *in vivo*. Fast 3D photoacoustic microscopy is anticipated to facilitate applications of photoacoustic imaging in biomedical studies that involve dynamics and clinical procedures that demand immediate diagnosis.

Noninvasive photoacoustic sentinel lymph node (SLN) mapping with high spatial resolution has the potential to improve the false negative rate and eliminate the use of radioactive tracers in SLN identification. In addition, high spatial resolution may enable physicians to replace SLN biopsy with fine needle aspiration biopsy, and thus reduce the risk of associated morbidity. In **Chapter 5**, we demonstrate the feasibility of high-speed 3D photoacoustic imaging of the uptake and clearance dynamics of Evans blue dye in SLNs. Upon injection of Evans blue, which is currently used in clinical SLN biopsy, SLNs in mice and rats are accurately and noninvasively mapped *in vivo* using our PAM system. In our experiments, the SLNs are found to be located at ~0.65 mm below the skin surface in mice and ~1.2 mm in rats. In some cases, lymph vessels and lymphatic valves are also imaged. The dye dynamics—accumulation and clearance—in SLNs are

quantitatively monitored by sequential 3D imaging with temporal resolution as high as ~6 s. The demonstrated capability suggests that high-speed 3D photoacoustic imaging should facilitate the understanding of the dynamics of various dyes in SLNs, and potentially help identify SLNs with high accuracy.

In **Chapter 6**, with a refined ultrasound-array-based real-time photoacoustic microscopy (UA-PAM) system, we demonstrate the feasibility of noninvasive *in vivo* imaging of human pulsatile dynamics. The system, capable of real-time B-scan imaging at 50 Hz and high-speed 3D imaging, is validated by imaging the subcutaneous microvasculature in rats and humans. After the validation, a human artery around the palm–wrist area is imaged, and its pulsatile dynamics, including the arterial pulsatile motion and changes in hemoglobin concentration, are monitored, with 20-ms B-scan imaging temporal resolution. To our knowledge, this is the first demonstration of real-time photoacoustic imaging of human physiological dynamics. Given the results achieved in this study, we believe that UA-PAM potentially offers many new possibilities for studying functional and physiological dynamics in both preclinical and clinical imaging settings.

In **Chapter 7**, we present a section-illumination photoacoustic microscopy system capable of dynamic *in vivo* imaging of microvessels as small as 30 micrometers in diameter. The section illumination improves the elevational resolution, while an ultrasound array provides the in-plane axial and lateral resolutions. Using the imaging system, we have monitored the wash-in dynamics of Evans Blue in the microcirculation of mouse ears at 249-Hz 2-D and 0.5-Hz 3-D image acquisition rates. Such observations allow us to differentiate the arterioles from the venules. In the future, the technology may be used to study angiogenesis, diabetes-induced vascular complications, and pharmacokinetics.

In **Chapter 8**, we present a multi-focal optical-resolution photoacoustic microscopy system capable of high-resolution imaging of both hemoglobin concentration and oxygenation in individual microvessels *in vivo* at high speed. A microlens array focuses laser light into multiple illumination beams for photoacoustic excitation; an ultrasound array detects the photoacoustic signals from the illumination beams, which are separated by lateral distances as small as the lateral resolution of the ultrasound array. Compared with a single focus, multiple foci reduce the scanning load and increase the imaging speed significantly. The current multi-focal system can acquire 1000 × 500 × 200 voxels at ~10-μm lateral resolution within only 4 min.

References

1. Zhang, H.F., Maslov, K., Stoica, G. & Wang, L.H.V. Functional photoacoustic microscopy for high-resolution and noninvasive *in vivo* imaging. *Nature Biotechnology* **24**, 848-851 (2006).
2. Wang, L.V. Multiscale photoacoustic microscopy and computed tomography. *Nature Photonics* **3**, 503-509 (2009).
3. Lagaru, A., Chen, X.Y. & Gambhir, S.S. Molecular imaging can accelerate anti-angiogenic drug development and testing. *Nature Clinical Practice Oncology* **4**, 556-557 (2007).
4. Weissleder, R. Scaling down imaging: Molecular mapping of cancer in mice. *Nature Reviews Cancer* **2**, 11-18 (2002).
5. Rudin, M. & Weissleder, R. Molecular imaging in drug discovery and development. *Nature Reviews Drug Discovery* **2**, 123-131 (2003).
6. Willmann, J.K., van Bruggen, N., Dinkelborg, L.M. & Gambhir, S.S. Molecular imaging in drug development. *Nature Reviews Drug Discovery* **7**, 591-607 (2008).
7. Helmchen, F. & Denk, W. Deep tissue two-photon microscopy. *Nature Methods* **2**, 932-940 (2005).
8. Antcliff, R.J. et al. Intravitreal triamcinolone for uveitic cystoid macular edema: An optical coherence tomography study. *Ophthalmology* **108**, 765-772 (2001).
9. Guedes, V. et al. Optical coherence tomography measurement of macular and nerve fiber layer thickness in normal and glaucomatous human eyes. *Ophthalmology* **110**, 177-189 (2003).

10. Suter, M.J., Tearney, G.J., Oh, W.Y. & Bouma, B.E. Progress in Intracoronary Optical Coherence Tomography. *Ieee Journal of Selected Topics in Quantum Electronics* **16**, 706-714 (2010).

11. Tanaka, A., Tearney, G.J. & Bouma, B.E. Challenges on the frontier of intracoronary imaging: atherosclerotic plaque macrophage measurement by optical coherence tomography. *Journal of Biomedical Optics* **15**, 011104 (2010).

12. Tearney, G.J., Jang, I.K. & Bouma, B.E. Optical coherence tomography for imaging the vulnerable plaque. *Journal of Biomedical Optics* **11**, 021002 (2006).

13. Webb, R.H. Confocal optical microscopy. *Reports on Progress in Physics* **59**, 427-471 (1996).

14. Huang, D. et al. Optical coherence tomography. *Science* **254**, 1178-1181 (1991).

15. Gibson, A.P., Hebden, J.C. & Arridge, S.R. Recent advances in diffuse optical imaging. *Physics in Medicine and Biology* **50**, R1-R43 (2005).

16. Bell, A.G. On the production and reproduction of sound by light. *Am. J. Sci.* **20**, 305-324 (1880).

17. Kruger, R.A., Liu, P.Y., Fang, Y.R. & Appledorn, C.R. Photoacoustic Ultrasound (Paus) - Reconstruction Tomography. *Medical Physics* **22**, 1605-1609 (1995).

18. Oraevsky, A.A., Jacques, S.L. & Tittel, F.K. Determination of tissue optical properties by piezoelectric detection of laser-induced stress waves. *Proc. SPIE* **1882**, 86-101 (1993).

19. Xu, M.H. & Wang, L.H.V. Photoacoustic imaging in biomedicine. *Review of Scientific Instruments* **77**, 041101 (2006).

20. Wang, L.V. & Wu, H.-I. Biomedical optics: principles and imaging. (John Wiley & Sons, Inc., Hoboken, New Jersey; 2007).

21. Denk, W., Strickler, J.H. & Webb, W.W. Two-photon laser scanning fluorescence microscopy. *Science* **248**, 73-76 (1990).

22. Wang, L.V. Prospects of photoacoustic tomography. *Medical Physics* **35**, 5758-5767 (2008).

23. Zhang, H.F., Maslov, K., Sivaramakrishnan, M., Stoica, G. & Wang, L.H.V. Imaging of hemoglobin oxygen saturation variations in single vessels *in vivo* using photoacoustic microscopy. *Applied Physics Letters* **90**, 053901 (2007).

24. Li, M.L. et al. Simultaneous molecular and hypoxia imaging of brain tumors *in vivo* using spectroscopic photoacoustic tomography. *Proceedings of the Ieee* **96**, 481-489 (2008).

25. Hu, S., Yan, P., Maslov, K., Lee, J.M. & Wang, L.H.V. Intravital imaging of amyloid plaques in a transgenic mouse model using optical-resolution photoacoustic microscopy. *Optics Letters* **34**, 3899-3901 (2009).

26. Zemp, R.J. et al. Photoacoustic imaging of the microvasculature with a high-frequency ultrasound array transducer. *Journal of Biomedical Optics* **12**, 010501 (2007).

27. Massoud, T.F. & Gambhir, S.S. Molecular imaging in living subjects: seeing fundamental biological processes in a new light. *Genes & Development* **17**, 545-580 (2003).

28. Abbey, C. et al. Longitudinal correlations in a small-animal PET studies. *Medical Physics* **32**, 1901-1901 (2005).

29. Dayton, P.A. & Ferrara, K.W. Targeted imaging using ultrasound. *Journal of Magnetic Resonance Imaging* **16**, 362-377 (2002).

30. Couture, O. et al. Investigating perfluorohexane particles with high-frequency ultrasound. *Ultrasound in Medicine and Biology* **32**, 73-82 (2006).

31. Dunn, A. & Boas, D. Transport-based image reconstruction in turbid media with small source-detector separations. *Optics Letters* **25**, 1777-1779 (2000).

32. Hillman, E.M.C., Boas, D.A., Dale, A.M. & Dunn, A.K. Laminar optical tomography: demonstration of millimeter-scale depth-resolved imaging in turbid media. *Optics Letters* **29**, 1650-1652 (2004).

33. Ku, G., Wang, X.D., Xie, X.Y., Stoica, G. & Wang, L.H.V. Imaging of tumor angiogenesis in rat brains *in vivo* by photoacoustic tomography. *Applied Optics* **44**, 770-775 (2005).

34. Wang, X.D. et al. Noninvasive laser-induced photoacoustic tomography for structural and functional *in vivo* imaging of the brain. *Nature Biotechnology* **21**, 803-806 (2003).

35. Maslov, K., Stoica, G. & Wang, L.V.H. *In vivo* dark-field reflection-mode photoacoustic microscopy. *Optics Letters* **30**, 625-627 (2005).

36. Sivaramakrishnan, M., Maslov, K., Zhang, H.F., Stoica, G. & Wang, L.V. Limitations of quantitative photoacoustic measurements of blood oxygenation in small vessels. *Physics in Medicine and Biology* **52**, 1349-1361 (2007).

37. Wang, X.D., Xie, X.Y., Ku, G.N. & Wang, L.H.V. Noninvasive imaging of hemoglobin concentration and oxygenation in the rat brain using high-resolution photoacoustic tomography. *Journal of Biomedical Optics* **11**, 024015 (2006).

38. Li, L., Zemp, R.J., Lungu, G., Stoica, G. & Wang, L.H.V. Photoacoustic imaging of lacZ gene expression *in vivo*. *Journal of Biomedical Optics* **12**, 020504 (2007).

39. Niederhauser, J.J., Jaeger, M., Lemor, R., Weber, P. & Frenz, M. Combined ultrasound and optoacoustic system for real-time high-contrast vascular imaging *in vivo*. *Ieee Transactions on Medical Imaging* **24**, 436-440 (2005).

40. Esenaliev, R.O., Karabutov, A.A. & Oraevsky, A.A. Sensitivity of laser opto-acoustic imaging in detection of small deeply embedded tumors. *Ieee Journal of Selected Topics in Quantum Electronics* **5**, 981-988 (1999).

41. Oraevsky, A.A., Jacques, S.L. & Tittel, F.K. Measurement of tissue optical properties by time-resolved detection of laser-induced transient stress. *Applied Optics* **36**, 402-415 (1997).

42. Kruger, R.A., Kiser, W.L., Reinecke, D.R. & Kruger, G.A. Thermoacoustic computed tomography using a conventional linear transducer array. *Medical Physics* **30**, 856-860 (2003).

43. Kruger, R., Kiser, W., Reinecke, D. & Kruger, G. Molecular imaging with thermoacoustic computed tomography. *Medical Physics* **30**, 1542-1542 (2003).

44. Zhang, E. & Beard, P. Broadband ultrasound field mapping system using a wavelength tuned, optically scanned focused laser beam to address a Fabry Perot polymer film sensor. *Ieee Transactions on Ultrasonics Ferroelectrics and Frequency Control* **53**, 1330-1338 (2006).

45. Zemp, R.J. et al. Photoacoustic imaging of the microvasculature with a high-frequency ultrasound array transducer. *J Biomed Opt* **12**, 010501 (2007).

46. Cannata, J.M., Williams, J.A., Zhou, Q.F., Ritter, T.A. & Shung, K.K. Development of a 35-MHz piezo-composite ultrasound array for medical imaging. *Ieee Transactions on Ultrasonics Ferroelectrics and Frequency Control* **53**, 224-236 (2006).

47. Bitton, R. et al. in Ultrasonics Symposium, 2006. IEEE 389-3922006).

48. Wall, K. & Lockwood, G.R. in Ultrasonics Symposium, 2005 IEEE, Vol. 2 1400-1403 (2005).

49. Development of a real-time, high-frequency ultrasound digital beamformer for high-frequency linear array transducers. *Ultrasonics, Ferroelectrics and Frequency Control, IEEE Transactions on* **53**, 317-323 (2006).

50. Moore, G.E. Cramming More Components Onto Integrated Circuits. *Proceedings of the IEEE* **86**, 82-85 (1998).

51. Napolitano, D. et al. in Ultrasonics, 2003 IEEE Symposium on, Vol. 1 25-28 Vol.21 (2003).

52. Foster, F.S. et al. A new ultrasound instrument for *in vivo* microimaging of mice. *Ultrasound in Medicine and Biology* **28**, 1165-1172 (2002).

53. Li, L., Zemp, R.J., Lungu, G., Stoica, G. & Wang, L.H.V. Photoacoustic imaging of lacZ gene expression *in vivo*. *Journal of Biomedical Optics* **12**, - (2007).

54. Zemp, R.J., Song, L., Bitton, R., Shung, K.K. & Wang, L.V. Realtime photoacoustic microscopy *in vivo* with a 30-MHz ultrasound array transducer. *Optics Express* **16**, 7915-7928 (2008).

55. Richards, A.G., Simonson, E. & Visscher, M.B. Electrocardiogram and Phonogram of Adult and Newborn Mice in Normal Conditions and Under the Effect of Cooling, Hypoxia and Potassium. *Am J Physiol* **174**, 293-298 (1953).

56. Kramer, K. et al. Use of Telemetry to Record Electrocardiogram and Heart-Rate in Freely Moving Mice. *Journal of Pharmacological and Toxicological Methods* **30**, 209-215 (1993).

57. Manohar, S. et al. Initial results of *in vivo* non-invasive cancer imaging in the human breast using near-infrared photoacoustics. *Optics Express* **15**, 12277-12285 (2007).

58. Oh, J.T. et al. Three-dimensional imaging of skin melanoma *in vivo* by dual-wavelength photoacoustic microscopy. *Journal of Biomedical Optics* **11**, 034032 (2006).

59. Yang, D.W., Xing, D., Yang, S.H. & Xiang, L.Z. Fast full-view photoacoustic imaging by combined scanning with a linear transducer array. *Optics Express* **15**, 15566-15575 (2007).

60. Wang, L.V., Nordquist, R.E. & Chen, W.R. Optimal beam size for light delivery to absorption-enhanced tumors buried in biological tissues and effect of multiple-beam delivery: A Monte Carlo study. *Applied Optics* **36**, 8286-8291 (1997).

61. American National Standard for Safe Use of Lasers (ANSI Z136.1-2000) (The Laser Institute of America, Orlando, FL; 2000).

62. Hu, C.H., Xu, X.C., Cannata, J.M., Yen, J.T. & Shung, K.K. Development of a real-time, high-frequency ultrasound digital beamformer for high-frequency linear array transducers. *Ieee Transactions on Ultrasonics Ferroelectrics and Frequency Control* **53**, 317-323 (2006).

63. Morton, D.L. et al. Technical details of intraoperative lymphatic mapping for early stage melanoma. *Arch Surg* **127**, 392-399 (1992).

64. Giuliano, A.E., Kirgan, D.M., Guenther, J.M. & Morton, D.L. Lymphatic mapping and sentinel lymphadenectomy for breast cancer. *Ann Surg* **220**, 391-398; discussion 398-401 (1994).

65. Schulze, T., Bembenek, A. & Schlag, P.M. Sentinel lymph node biopsy progress in surgical treatment of cancer. *Langenbecks Arch Surg* **389**, 532-550 (2004).

66. Mariani, G. et al. Radioguided sentinel lymph node biopsy in breast cancer surgery. *J Nucl Med* **42**, 1198-1215 (2001).

67. Schirrmeister, H. et al. Prospective evaluation of factors influencing success rates of sentinel node biopsy in 814 breast cancer patients. *Cancer Biother Radiopharm* **19**, 784-790 (2004).

68. McMasters, K.M. et al. Sentinel lymph node biopsy for breast cancer: a suitable alternative to routine axillary dissection in multi-institutional practice when optimal technique is used. *J Clin Oncol* **18**, 2560-2566 (2000).

69. Ung, O.A. Australasian experience and trials in sentinel lymph node biopsy: the RACS SNAC trial. *Asian J Surg* **27**, 284-290 (2004).

70. Purushotham, A.D. et al. Morbidity after sentinel lymph node biopsy in primary breast cancer: results from a randomized controlled trial. *J Clin Oncol* **23**, 4312-4321 (2005).

71. Krishnamurthy, S. et al. Role of ultrasound-guided fine-needle aspiration of indeterminate and suspicious axillary lymph nodes in the initial staging of breast carcinoma. *Cancer* **95**, 982-988 (2002).

72. Koelliker, S.L., Chung, M.A., Mainiero, M.B., Steinhoff, M.M. & Cady, B. Axillary lymph nodes: US-guided fine-needle aspiration for initial staging of breast cancer--correlation with primary tumor size. *Radiology* **246**, 81-89 (2008).

73. Sharma, R. et al. Quantitative imaging of lymph function. *Am J Physiol Heart Circ Physiol* **292**, H3109-3118 (2007).

74. Kim, S. et al. Near-infrared fluorescent type II quantum dots for sentinel lymph node mapping. *Nat Biotechnol* **22**, 93-97 (2004).

75. Kwon, S. & Sevick-Muraca, E.M. Noninvasive quantitative imaging of lymph function in mice. *Lymphat Res Biol* **5**, 219-231 (2007).

76. Sevick-Muraca, E.M. et al. Imaging of lymph flow in breast cancer patients after microdose administration of a near-infrared fluorophore: feasibility study. *Radiology* **246**, 734-741 (2008).

77. Ohnishi, S. et al. Organic alternatives to quantum dots for intraoperative near-infrared fluorescent sentinel lymph node mapping. *Mol Imaging* **4**, 172-181 (2005).

78. Song, K.H. & Wang, L.V. Deep reflection-mode photoacoustic imaging of biological tissue. *J Biomed Opt* **12**, 060503 (2007).

79. *The depths of the SLNs were measured by axillary ultrasonography. We analyzed ultrasound breast images of 24 patients to extract the statistics about the depth and size of SLNs.*

80. Song, K.H., Stein, E.W., Margenthaler, J.A. & Wang, L.V. Noninvasive photoacoustic identification of sentinel lymph nodes containing methylene blue *in vivo* in a rat model. *J Biomed Opt* **13**, 054033 (2008).

81. Song, K.H., Kim, C., Cobley, C.M., Xia, Y. & Wang, L.V. Near-infrared gold nanocages as a new class of tracers for photoacoustic sentinel lymph node mapping on a rat model. *Nano Lett* **9**, 183-188 (2009).

82. Song, L., Maslov, K., Bitton, R., Shung, K.K. & Wang, L.V. Fast 3-D dark-field reflection-mode photoacoustic microscopy *in vivo* with a 30-MHz ultrasound linear array. *J Biomed Opt* **13**, 054028 (2008).

83. Zemp, R.J., Song, L., Bitton, R., Shung, K.K. & Wang, L.V. Realtime photoacoustic microscopy *in vivo* with a 30-MHz ultrasound array transducer. *Opt Express* **16**, 7915-7928 (2008).

84. Zemp, R.J., Song, L., Bitton, R., Shung, K.K. & Wang, L.V. Realtime photoacoustic microscopy of murine cardiovascular dynamics. *Opt Express* **16**, 18551-18556 (2008).

85. Bobin, J.Y., Zinzindohoue, C., Isaac, S., Saadat, M. & Roy, P. Tagging sentinel lymph nodes: a study of 100 patients with breast cancer. *Eur J Cancer* **35**, 569-573 (1999).

86. Bobin, J.Y. et al. [Lymph node mapping and axillary sentinel lymph node biopsy in 243 invasive breast cancers with no palpable nodes. The south Lyon hospital center experience]. *Ann Chir* **125**, 861-870 (2000).

87. Patterson, C.E., Rhoades, R.A. & Garcia, J.G.N. Evans Blue-Dye as a Marker of Albumin Clearance in Cultured Endothelial Monolayer and Isolated Lung. *Journal of Applied Physiology* **72**, 865-873 (1992).

88. Wang, L.-H.V. & Wu, H. Biomedical optics: principles and imaging. (Wiley, Hoboken, New Jersey 2007).

89. Maslov, K., Stoica, G. & Wang, L.V. *In vivo* dark-field reflection-mode photoacoustic microscopy. *Opt Lett* **30**, 625-627 (2005).

90. Zhang, H.F., Maslov, K. & Wang, L.V. *In vivo* imaging of subcutaneous structures using functional photoacoustic microscopy. *Nat Protoc* **2**, 797-804 (2007).

91. Zhang, H.F., Maslov, K., Stoica, G. & Wang, L.V. Functional photoacoustic microscopy for high-resolution and noninvasive *in vivo* imaging. *Nat Biotechnol* **24**, 848-851 (2006).

92. Laser Institute of America, American National Standard for Safe Use of Lasers ANSI Z136.1-2000 (American National Standards Institute, Inc., New York, NY, 2000).

93. Roggan, A., Friebel, M., Dorschel, K., Hahn, A. & Muller, G. Optical properties of circulating human blood in the wavelength range 400-2500 NM. *Journal of Biomedical Optics* **4**, 36-46 (1999).

94. Heidemann, R.M. et al. A brief review of parallel magnetic resonance imaging. *Eur Radiol* **13**, 2323-2337 (2003).

95. Wells, P.N.T. Ultrasound imaging. *Phys Med Biol* **51**, R83-R98 (2006).

96. Webb, R.H. Confocal optical microscopy. *Rep Prog Phys* **59**, 427-471 (1996).

97. Huang, D. et al. Optical Coherence Tomography. *Science* **254**, 1178-1181 (1991).

98. Song, L., Kim, C., Maslov, K., Shung, K.K. & Wang, L.H.V. High-speed dynamic 3D photoacoustic imaging of sentinel lymph node in a murine model using an ultrasound array. *Medical Physics* **36**, 3724-3729 (2009).

99. Song, L., Maslov, K., Bitton, R., Shung, K.K. & Wang, L.V. Fast 3-D dark-field reflection-mode photoacoustic microscopy *in vivo* with a 30-MHz ultrasound linear array. *Journal of Biomedical Optics* **13**, 054028 (2008).

100. Leahya, M.J. et al. Biophotonic methods in microcirculation imaging. *Medical Laser Application* **22**, 105-126 (2007).

101. Stern, M.D. *In vivo* evaluation of microcirculation by coherent light scattering. *Nature* **254**, 56-58 (1975).

102. Groner, W. et al. Orthogonal polarization spectral imaging: A new method for study of the microcirculation. *Nature Medicine* **5**, 1209-1213 (1999).

103. DeVries, A.F. et al. Tumor microcirculation evaluated by dynamic magnetic resonance imaging predicts therapy outcome for primary rectal carcinoma. *Cancer Research* **61**, 2513-2516 (2001).

104. Cutolo, M., Sulli, A., Pizzorni, C. & Accardo, S. Nailfold videocapillaroscopy assessment of microvascular damage in systemic sclerosis. *Journal of Rheumatology* **27**, 155-160 (2000).

105. Goertz, D.E., Yu, J.L., Kerbel, R.S., Burns, P.N. & Foster, F.S. High-frequency 3-D color-flow imaging of the microcirculation. *Ultrasound in Medicine and Biology* **29**, 39-51 (2003).

106. Maslov, K., Zhang, H.F., Hu, S. & Wang, L.V. Optical-resolution photoacoustic microscopy for *in vivo* imaging of single capillaries. *Optics Letters* **33**, 929-931 (2008).

107. Song, L., Maslov, K., Shung, K.K. & Wang, L.H.V. Ultrasound-array-based real-time photoacoustic microscopy of human pulsatile dynamics *in vivo*. *Journal of Biomedical Optics* **15**, 021303 (2010).

108. Hu, S., Maslov, K. & Wang, L.H.V. Noninvasive label-free imaging of microhemodynamics by optical-resolution photoacoustic microscopy. *Optics Express* **17**, 7688-7693 (2009).

109. Chaigneau, E., Oheim, M., Audinat, E. & Charpak, S. Two-photon imaging of capillary blood flow in olfactory bulb glomeruli. *Proceedings of the National Academy of Sciences of the United States of America* **100**, 13081-13086 (2003).

110. Laemmel, E. et al. Fibered confocal fluorescence microscopy (Cell-viZio (TM)) facilitates extended imaging in the field of microcirculation - A comparison with intravital microscopy. *Journal of Vascular Research* **41**, 400-411 (2004).

111. Schaffer, C.B. et al. Two-photon imaging of cortical surface microvessels reveals a robust redistribution in blood flow after vascular occlusion. *Plos Biology* **4**, 258-270 (2006).

112. Wang, R.K. & An, L. Doppler optical micro-angiography for volumetric imaging of vascular perfusion *in vivo*. *Optics Express* **17**, 8926-8940 (2009).

113. Hu, S. & Wang, L.V. Photoacoustic imaging and characterization of the microvasculature. *Journal of Biomedical Optics* **15**, 011101 (2010).

114. Hu, S., Maslov, K. & Wang, L.H.V. *In vivo* functional chronic imaging of a small animal model using optical-resolution photoacoustic microscopy. *Medical Physics* **36**, 2320-2323 (2009).

115. Xie, Z.X., Jiao, S.L., Zhang, H.F. & Puliafito, C.A. Laser-scanning optical-resolution photoacoustic microscopy. *Optics Letters* **34**, 1771-1773 (2009).

116. Rao, B., Li, L., Maslov, K. & Wang, L.H. Hybrid-scanning optical-resolution photoacoustic microscopy for *in vivo* vasculature imaging. *Optics Letters* **35**, 1521-1523 (2010).

117. Song, L., Maslov, K. & Wang, L.V. Section-illumination photoacoustic microscopy for dynamic 3D imaging of microcirculation *in vivo*. *Optics Letters* **35**, 1482-1484 (2010).